

## ABSTRACT

Title of Document:                   STRUCTURE AND PROPERTIES OF  
  NANOCOMPOSITES CONTAINING  
  ANISOTROPIC NANOPARTICLES

Bani Hans Cipriano, Doctor of  
Philosophy, 2007

Directed By:                         Professor Srinivasa R. Raghavan, Department of  
  Chemical and Biomolecular Engineering

This dissertation deals with polymeric materials containing dispersed anisotropic nanoparticles such as nanotubes, nanofibers, and nanoplatelets. Such polymer nanocomposites have attracted much attention since they exhibit a host of superior properties over the parent polymer. For example, nanoparticles can impart flame-retardancy, high electrical conductivities, and high mechanical stiffness to the polymer. Despite the growing interest in these materials, many aspects remain poorly characterized, and the connection between properties and microstructure is still not fully understood. This provides the motivation for the present study.

In the first part of this study, we focus on the flammability behavior of polymer nanocomposites containing multi-walled carbon nanotubes (MWNTs). It has been shown that MWNTs impart flame-retardancy to the polymer at low loadings, and moreover, the

flame-retardancy correlates with the rheological properties of the nanocomposite. Here, we show that the *aspect ratio* of MWNTs is a key parameter in controlling both the rheology and flammability. Particles with a larger aspect ratio impart much higher storage moduli and complex viscosities to the nanocomposites compared to equivalent mass loadings of particles with a smaller aspect ratio. Additionally, in flammability experiments, the larger-aspect-ratio particles lead to a greater reduction in mass loss rate, i.e., they are more effective at reducing flammability.

In the second part of this study, we focus on the conductivity of nanocomposites containing particles such as MWNTs or carbon nanofibers (CNFs). When these materials are processed by compression molding or melt extrusion, the conductivities of the resulting composites are often found to be disappointingly low. Here, we show that the conductivities can be increased, sometimes by orders of magnitude, simply by subjecting the sample to quiescent annealing at temperatures above the polymer's glass transition temperature ( $T_g$ ). We demonstrate these results for both MWNT and CNF-based composites in polystyrene (PS). The mechanism behind the conductivity increase is shown to involve an increase in the connectivity of the particle network, which is reflected in dynamic rheological measurements as an increase in the plateau modulus at low frequencies.

In the final part of this study, we present a simple method to improve the rheology and flammability properties of nanocomposites formed from polymers and clay platelets. These materials are usually made by combining a polymer with a commercial organoclay

powder. We show that by fractionating the clay to exclude low-aspect ratio particles and aggregates, we can improve their dispersion (exfoliation) in the polymer. The resulting composites have higher optical transparency and better rheological properties for a given mass loading of clay. When these composites are subjected to a flame, we find a more uniform residue when compared to samples with the commercial organoclay. The fractionated clay also shows an interesting behavior when dispersed in water, where it forms birefringent gels at high particle loadings.

**STRUCTURE AND PROPERTIES OF POLYMER  
NANOCOMPOSITES CONTAINING ANISOTROPIC  
NANOPARTICLES**

By

Bani Hans Cipriano

Dissertation submitted to the Faculty of the Graduate School of the  
University of Maryland, College Park, in partial fulfillment  
of the requirements for the degree of  
Doctor of Philosophy  
2007

Advisory Committee:

Prof. Srinivasa R. Raghavan, Dept. of Chemical & Biomolecular Eng., Chair

Prof. Sheryl H. Ehrman, Dept. of Chemical & Biomolecular Engineering

Prof. Takashi Kashiwagi, Dept. of Fire Protection Engineering

Prof. Robert M. Briber, Dept. of Materials Science & Engineering

Prof. Peter Kofinas, Dept. of Bioengineering

Prof. Joseph F. Schork, Dept. of Chemical & Biomolecular Eng.

© Copyright by  
Bani Hans Cipriano  
2007

This dissertation is dedicated to my parents, Cruz Cipriano y Rubidia de Cipriano, and to my brother, Aaron F. Cipriano. A pesar de la distancia y el tiempo que nos han separado, nunca duden que les quiero mucho.

## ACKNOWLEDGEMENTS

This dissertation was made possible by the support and guidance of Dr. Srinivasa R. Raghavan. As my Ph. D. advisor, he encouraged me to pursue several avenues of materials research. He is a fierce proponent of good scientific story telling through data, pictures and movies alike; his influence can be seen throughout this work. On a personal level, I value his friendship and admire his dedication. Thanks for caring.

In addition, I would like to acknowledge Dr. Takashi Kashiwagi with whom Srini and I have had a fruitful collaboration over the last five years. I consider him my co-advisor. Thank you for always having the time to share ideas and discuss research.

The Complex Fluids and Nanomaterials group, of which Srini is the principal investigator, deserves my gratitude. The last five years of my life were great in part because of this very special group of people. I'm very proud of the fact that a group of us won a prize in the business plan competition and founded a company. This achievement exemplifies the level of dedication, technical competence and enthusiasm of my group members. However, above all I will always cherish the everyday spontaneity and friendship of my group members. Whether lunch at Chipotle or Gah Ram, somehow when you guys were around the food tasted much better. I hope that our friendship will continue.

I also acknowledge the assistance of Mr. Richard Harris who conducted XRD measurements and prepared PS/MWNT by extrusion. Mr. Arun Kota and Dr. Hugh

Bruck of Mechanical Engineering performed electrical conductivity, thermogravimetric analysis measurements and PS/CNF extrusion. Furthermore, Mr. Xin Zhang of Materials Engineering obtained the TEM images of the nanocomposites in Chapter 5. This work was funded by a grant from NIST BFRL.

I wish to thank my extended family living in Maryland. Without Nelson and Miriam; Alex; and Sara and Ricardo this work would not have been possible. I am forever indebted to you for your company and encouragement during difficult times as well as for welcoming me to your homes. Furthermore, I would like to acknowledge the congregation of the Wheaton Spanish Seventh Day Adventist Church. Lastly, Sylvia Garcia encouraged me during the final months of this endeavor.

Finally, as Chris Macosko put it in *Rheology: Principles, Measurements and Applications*, the Source of inspiration for this work is the same that inspired far greater scientists. “From Him who created all, flow life and light and gladness, throughout the realms of illimitable space. From the minutest atom to the greatest world, all things, animate and inanimate, in their unshadowed beauty and perfect joy, declare that God is love.” – *The Great Controversy* by Ellen H. White.

Kensington, MD

September 2007

# TABLE OF CONTENTS

	<i>Page</i>
<b>Dedication</b> .....	ii
<b>Acknowledgements</b> .....	iii
<b>Table of Contents</b> .....	v
<b>List of Figures</b> .....	vii
<b>1. Introduction and Overview</b> .....	1
<b>2. Background</b> .....	5
2.1. Carbon Nanotubes .....	5
2.2. Carbon Nanofibers .....	6
2.3. Clay Particles .....	7
2.4. Polymer Nanocomposites .....	9
2.5. Rheological Properties and Their Measurement .....	10
2.6. Flammability Properties and Their Measurement .....	13
2.7. Electrical Conductivity and Its Measurement .....	15
<b>3. Effect of Aspect Ratio of MWNTs on Nanocomposite Properties</b> .....	17
3.1. Introduction .....	17
3.2. Experimental.....	19
3.3. Results and Discussion .....	22
3.3.1. MWNT Aspect Ratio and Morphology of Nanocomposites .....	22
3.3.2. Thermal Stability .....	24
3.3.3. Viscoelastic Properties .....	25
3.3.4. Flammability Behavior .....	29
3.4. Discussion .....	32
3.5. Conclusions .....	36
<b>4. Recovery of Nanocomposite Properties by Annealing</b> .....	37
4.1. Introduction .....	37
4.2. Experimental .....	39
4.3. Results .....	41

4.3.1. Electrical Conductivity .....	41
4.3.2. Dynamic Rheology .....	44
4.3.3. Confocal Microscopy .....	46
4.4. Discussion .....	47
4.5. Conclusions .....	49
<b>5. Effect of Clay Fractionation on Nanocomposite Properties .....</b>	<b>51</b>
5.1. Introduction .....	51
5.2. Experimental .....	53
5.3. Results and Discussion .....	57
5.3.1. Clay Fractions in Water .....	57
5.3.2. Nanocomposite Morphology .....	60
5.3.3. Nanocomposite Transparency .....	62
5.3.4. Viscoelastic Properties .....	63
5.3.5. Flammability .....	65
5.5. Conclusions .....	67
<b>6. Conclusions and Recommendations .....</b>	<b>69</b>
6.1. Conclusions .....	69
6.2. Recommendations for Future Work .....	71
6.2.1. Flammability of Char Forming Polymers Containing MWNTs .....	71
6.2.2. Properties of o-FMT Nanocomposites .....	71
6.2.3. Dispersions of o-FMT in Non-Polar Solvents .....	72
<b>7. References .....</b>	<b>73</b>

# LIST OF FIGURES

**Figure 1.1.** Flammability of a polymer and its nanocomposites. Cone calorimetry data are shown for a PS melt and for PS nanocomposites with two different types of nanoparticle fillers: clay platelets at 5 wt% MWNTs at 2 wt%. The lower heat release rate for the nanocomposites indicates that they are much less flammable than the control polymer. In other words, the nanoparticle fillers are able to impart flame retardancy to the parent polymer. 2

**Figure 2.1.** Structure of SWNTs and MWNTs. (a) SWNTs are formed by rolling up a sheet of graphite and are classified based on their conformation as zigzag, chiral, or armchair structures. (b) High-resolution TEM image of an individual MWNT, clearly showing the multiple walls. 6

**Figure 2.2.** Structure of carbon nanofibers. (a) Schematic of a carbon nanofiber showing concentrically arranged graphite sheets in the core. (b) TEM image of the concentric graphite sheets. (c) Arrangement of graphite sheets in the nanofiber core is changed from concentric to random after heat treatment to 3000°C. (d) “Sword-in-sheath” failure mode can be observed in this carbon fiber; random arrangement of graphite sheets acts to decrease this mode of failure. 7

**Figure 2.3.** Schematics of native and organophilic clay. (a) Native montmorillonite showing a stack of two platelets. Each platelet is composed of three sheets, with two silicate sheets sandwiching an alumina sheet. The gallery spacing between the two platelets is about 12 Å. (b) Organophilic montmorillonite, obtained by treating the native clay with a cationic double-tailed surfactant, shown as molecules with a blue head and two red tails. The surfactant replaces the Na<sup>+</sup> cations and its tails are directed outwards from the clay surface. The gallery spacing between the platelets in a stack consequently increases to ca. 20 Å. 8

**Figure 2.4.** Schematics of the different morphologies of polymer-clay nanocomposites. 10

**Figure 2.5.** Schematic of the radiant gasification apparatus constructed at NIST to study the condensed phase processes during burning. 14

**Figure 3.1.** TEM images of the MWNTs extracted from the composites, left is MWNTs in the PS/MWNT prepared at University of Kentucky and right is MWNTs in the PS/MWNT compounded with the Hyperion master batch. 23

**Figure 3.2.** Confocal microscopy images with a scale bar of 20 μm : (a) PS/MWNT-150 (1%), (b) PS/MWNT-150 (2%), (c) PS/MWNT-150 (4%), (d) PS/MWNT-49 (1%), (e) PS/MWNT-49 (2%), (f) PS/MWNT-49 (4%). 24

**Figure 3.3.** Derivative thermogravimetric mass loss rates of selected samples. 25

- Figure 3.4.** Effects of aspect ratio and of mass concentration of MWNT on storage modulus of PS/MWNT nanocomposites at 200 °C. 26
- Figure 3.5.** The relationship between mass concentration of MWNT and normalized storage modulus of PS/MWNT nanocomposites at a frequency of 0.05 rad/s and 200 °C with that of PS. Insert is the power law relationship between the normalized storage modulus and normalized mass concentration of MWNT with percolation mass concentration  $P_c$ . 27
- Figure 3.6.** Effects of aspect ratio and of mass concentration of MWNT on complex viscosity of PS/MWNT nanocomposites at 200 °C. 28
- Figure 3.7.** Effects of mass concentration of MWNT on mass loss rate of PS/MWNT nanocomposites at 50 kW/m<sup>2</sup> in nitrogen. (a) Samples with MWNT-150 and (b) with MWNT-49. 29
- Figure 3.8.** Comparison of residues of PS/MWNT nanocomposites, based on MWNT-150 and MWNT-49, collected after the gasification test at 50 kW/m<sup>2</sup> in nitrogen. 31
- Figure 3.9.** The effects of aspect ratio of MWNT on the relationship between mass loss rate peak and mass concentration of MWNT. 32
- Figure 3.11.** Effects of clay type on mass loss rate of PP(92.3%)/PPgMA(7.7%) and PP(84.6%)/PPgMA(7.7%)/clay(7.7%) samples in nitrogen at 50 kW/m<sup>2</sup>. 34
- Figure 4.1.** Effect of annealing temperature on electrical conductivity: (a) PS/MWNT and (b) PS/CNF. Samples were annealed for 30 minutes. Note the increase of many orders of magnitude in electrical conductivity. 42
- Figure 4.2.** Effect of annealing time on electrical conductivity: (a) PS/MWNT annealed at 230 °C and (b) PS/CNF annealed at 200 °C. It takes longer to recover conductivity at low filler concentrations. 43
- Figure 4.3.** Effect of annealing on the dynamic rheological properties at 200°C of PS/CNT nanocomposites containing (a) 1 wt.% CNT and (b) 4 wt.% CNT. Data are shown for the elastic modulus  $G'$  (circles) and the viscous modulus  $G''$  (triangles) as functions of the frequency  $\omega$  for an unannealed sample (open symbols) and a sample annealed at 230°C for 30 min (filled symbols). In each case,  $G'$  at low  $\omega$  is increased by annealing, as shown by the arrows. 44
- Figure 4.4.** Confocal microscopy images showing the effect of annealing on the microstructure of PS/CNF nanocomposites containing 3 wt.% CNF. (a) Unannealed sample, showing alignment of CNFs, as confirmed by the elongated Fourier transform of this image, shown on the right. (b) Annealed sample, showing a more isotropic

orientation of the CNFs, as also seen from the isotropic shape of the Fourier transform image on the right. 47

**Figure 5.1.** Comparison of aqueous dispersions of FMT and LMT. LMT forms gels around 11%, whereas FMT gives rise to gels at 7%, based on the tube inversion test (top). Under crossed polarizers, the 7% FMT gel displays birefringence. 57

**Figure 5.2.** Optical microscopy images of aqueous dispersions of FMT (left) and LMT (right). Despite being larger in size, the effective aspect ratio in FMT dispersions is lowered by the formation of aggregates which can be seen in the image. Left: FMT. Right: LMT. 58

**Figure 5.3.** TEM images of FMT (left) and LMT (right). The particles were dried on the grid from their dilute aqueous dispersions. 59

**Figure 5.4.** XRD spectra for nanocomposites containing 5 weight % organoclay. Both nanocomposites have an intercalated morphology and the effect of clay size on polymer intercalation is negligible. 60

**Figure 5.5.** TEM images for nanocomposites containing 5% organoclay: (a) and (b) PS/o-FMT; (c) and (d) PS/15A. 61

**Figure 5.6.** Transmission of visible light through 200 mm thick nanocomposite films of PS/o-FMT (dashed line) and PS/15A (solid line). The transmission is higher across the wavelength range for samples containing o-FMT than for those containing 15A. 62

**Figure 5.7.** Dynamic rheology at 180°C of PS nanocomposites containing o-FMT and 15A. The elastic modulus  $G'$  is much higher for the o-FMT samples at the same loading. 63

**Figure 5.8.** Complex viscosity data for nanocomposites containing o-FMT and 15A. The o-FMT nanocomposites display higher values of complex viscosity than those prepared with 15A at the same loading. 64

**Figure 5.9.** (a) Mass loss rate of PS/o-FMT and PS/15A. The nanocomposites containing o-FMT display lower values of mass loss rate, about 20%. (b) Heat release rate profiles for both types of composites. 65

**Figure 5.10.** Residues of PS/15A and PS/o-FMT after a gasification experiment. Residues of samples containing o-FMT exhibit larger islands or lesser cracks; conversely, less of the aluminum pan is visible in the FMT residue images. 66

# Chapter 1

## INTRODUCTION AND OVERVIEW

This study seeks to characterize composite materials made by dispersing anisotropic nanoscale particles in polymeric matrices. These “polymer nanocomposites” have been the focus of much attention since improvement in mechanical and gas barrier properties can be achieved even with small loadings of the anisotropic particles.<sup>1</sup> In comparison, similar property improvements are possible only with much higher loadings of isotropic filler particles. The orientation of anisotropic particles in these nanocomposites may also be modulated by shear. Composites with aligned nanoparticles tend to show some of the same properties as liquid crystalline polymers (LCPs), while being much easier and inexpensive to synthesize.<sup>2</sup> Thus, aligned nanocomposites could replace LCPs in certain applications.

Our research in polymer nanocomposites began as a collaboration with the Building and Fire Research Laboratory (BFRL) at the National Institute of Standards and Technology (NIST) in Gaithersburg, MD. Researchers at BFRL have shown that anisotropic particles can also confer an additional useful property to polymers, which is that they make the polymer more *flame-retardant*.<sup>3</sup> Flammability is known to be an inherent problem with most thermoplastic polymers, and therefore, for these to be used in applications, additives that impart flame retardance (FR) must be added to the polymer. Indeed, more than 10 wt% of typical commercial polymers may be comprised of FR

additives (typically halogenated or phosphorus-containing compounds).<sup>4</sup> At such loadings, the FR additives tend to adversely affect many polymer properties, including the mechanical properties and clarity, and the use of these additives also raises environmental concerns. Given the current state-of-the-art, nanoparticles could present an attractive alternative as an FR additive. As mentioned earlier, nanoparticles tend to improve, not worsen, the mechanical properties. Moreover, BFRL researchers have shown that the *more anisotropic the nanoparticle, the lower the amount needed to achieve the FR effect*. This aspect is discussed in more detail below.

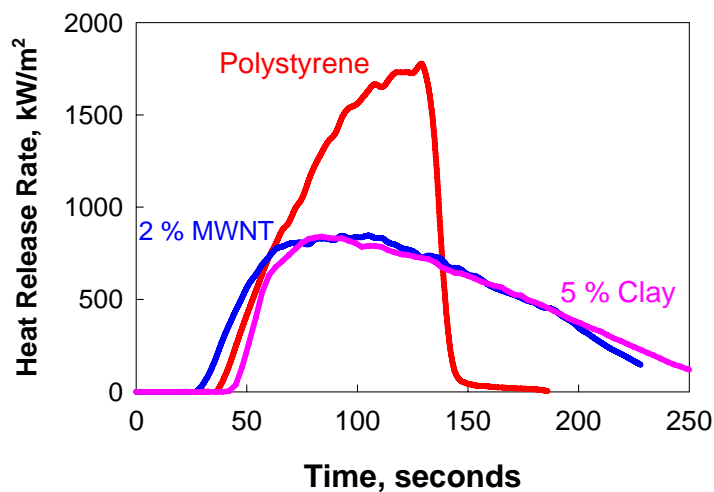


**Figure 1.1.** Flammability of a polymer and its nanocomposites. Cone calorimetry data are shown for a PS melt and for PS nanocomposites with two different types of nanoparticle fillers: clay platelets at 5 wt% MWNTs at 2 wt%. The lower heat release rate for the nanocomposites indicates that they are much less flammable than the control polymer. In other words, the nanoparticle fillers are able to impart flame retardancy to the parent polymer.

Figure 1.1 shows cone calorimetry data for the burning of a polystyrene (PS) melt with two different types of nanoparticle additives – clay platelets and multi-walled carbon

nanotubes (MWNTs). Cone calorimetry measures the heat released from the material when subjected to a flame, and a smaller amount of heat released corresponds to lower flammability. The data show that adding just 5 wt% of clay or 2 wt% of MWNTs imparts significant flame retardance to the material. The MWNTs have a greater degree of anisotropy compared to the clay platelets, which explains why a smaller amount of MWNTs is needed to achieve the FR effect. Recent studies at NIST BFRL have shown that the FR properties are strongly correlated with improvements in the rheological properties of the composite.<sup>3</sup> In other words, nanoparticle addition simultaneously makes the polymer both stronger *and* flame-retardant.

The above discussion highlights the unique combination of properties that are possible for polymer nanocomposites, which justifies the considerable scientific and technological attention given to these materials. This field is still a relatively young one, with most of the scientific reports having appeared only over the last 10-15 years or so. New types of nanoparticle additives, notably the carbon nanotubes, have become widely available only over the last few years. Much remains to be understood about the structure and properties of nanocomposites, and this provides the motivation for our study.

Our overall objectives in this study are to further our understanding of polymer nanocomposites in terms of structure and properties such as rheology, flammability, transparency and electrical conductivity. We study nanocomposites based on a variety of anisotropic nanoparticles, including multi-walled carbon nanotubes (MWNTs), clay platelets (montmorillonites), as well as carbon nanofibers (CNFs). The structure of the

resulting nanocomposites is characterized using diffraction and microscopic techniques. The rheological properties are studied under dynamic shear and the electrical conductivities are also measured. Finally, we also determine the flame-retardance of these materials at NIST BFRL in collaboration with Dr. Takashi Kashiwagi.

The studies conducted under this dissertation are organized into three chapters as follows. One general variable of interest is the particle size and aspect ratio, and this is a recurring theme in Chapters 3 and 5. In Chapter 3, we study the effect of MWNT aspect ratio on the flammability and rheology. We show that particles with larger aspect ratio provide a greater enhancement of properties. Chapter 4 studies the detrimental effect of bulk processing on the properties (especially the electrical conductivity) of composites made with MWNTs or CNFs. We show that the properties can be recovered by quiescent annealing of the material at high temperatures. Finally, Chapter 5 studies the effect of fractionating clay platelets on the properties of nanocomposites made from these particles. We show that the elimination of large aggregates greatly improves the rheology and transparency of these materials.

We expect that our work will have both scientific and technological relevance. Our essential contribution is to present design rules for nanocomposites in which several properties, such as flame-retardancy and rheology, are simultaneously improved. Moreover, our studies provide guidelines for the efficient manufacture of nanocomposites using bulk processing techniques, such as for the case of conductive MWNT or CNF-based materials.

# Chapter 2

## BACKGROUND

In this chapter, we describe the main properties of the nanoparticles that we will investigate in our work, and we will also discuss the behavior of polymer nanocomposites based on these particles. We will finish with a brief discussion of various techniques.

### 2.1. CARBON NANOTUBES

Carbon nanotubes (CNTs) can be considered to be rolled-up sheets of graphite.<sup>5,6</sup> When only one sheet is rolled up, it gives rise to single-walled nanotubes (SWNTs), whereas when many such sheets are rolled up, one inside the other, multi-walled nanotubes (MWNTs) are produced. Typical diameters of SWNTs range from 1–2 nm while they can be as long as several microns. MWNTs, on the other hand, have diameters of 20-75 nm and lengths up to ca. 50 microns. SWNTs can be classified according to their helicity, which depends on the angle at which the graphite sheet is rolled up. Based on helicity, SWNTs can exist as arm-chair, zig-zag or chiral as shown in Figure 2.1. Arm-chair and chiral SWNTs have metallic character whereas zig-zag SWNTs are semiconducting structures. Many applications of CNTs are predicated on their exceptional thermal and electrical conductivities. For instance, the thermal conductivity of SWNTs is about twice that of diamond while their current carrying capacity is expected to be a thousand times larger than that of copper wires. Furthermore, adding SWNTs or MWNTs to polymer matrices can increase their electrical conductivity by many orders of magnitude.

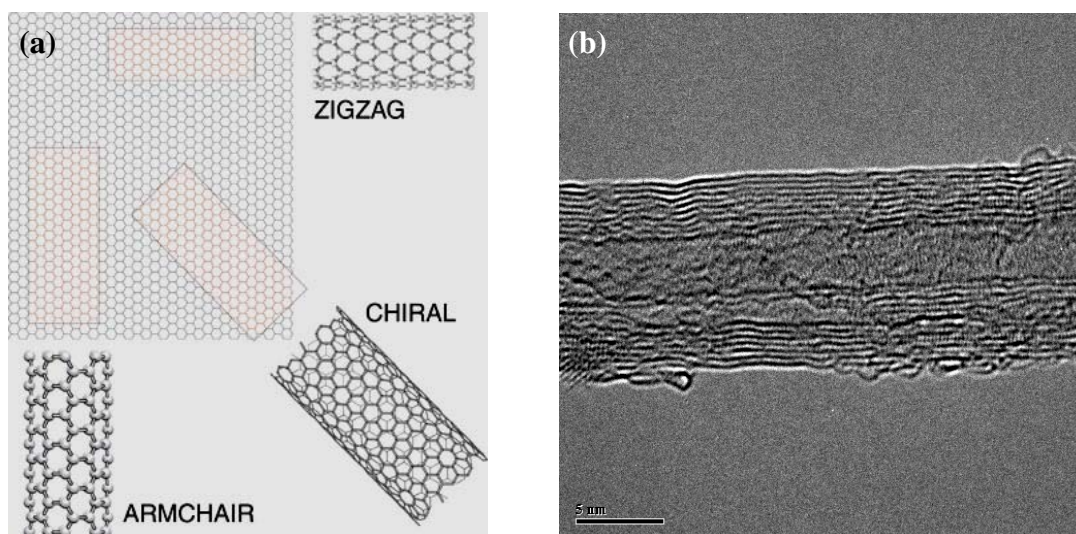


**Figure 2.1.** Structure of SWNTs and MWNTs. (a) SWNTs are formed by rolling up a sheet of graphite and are classified based on their conformation as zigzag, chiral, or armchair structures. (b) High-resolution TEM image of an individual MWNT, clearly showing the multiple walls.

## 2.2. CARBON NANOFIBERS

Carbon nanofibers (CNFs) are graphite-derived materials that are closely related to CNTs. They range in diameter from 100 to 1000 nm and their properties are similar to those of MWNTs. CNFs are typically produced in a vapor growth process wherein a hydrocarbon gas is made to react with finely milled Fe catalyst in a furnace at a temperature of 1100°C.<sup>6</sup> MWNTs are formed in the furnace initially, but this stage is followed by a fiber thickening process; if the reaction is stopped quickly, only MWNTs are grown. The diameter of the fibers can be controlled by limiting the extent of the thickening step. The as-produced fibers may be graphitized by heat treatment to 2500 °C in argon. The graphite sheets in the fiber core form a concentric arrangement, but this can be randomized by heat treating the fibers to 3000 °C in argon.

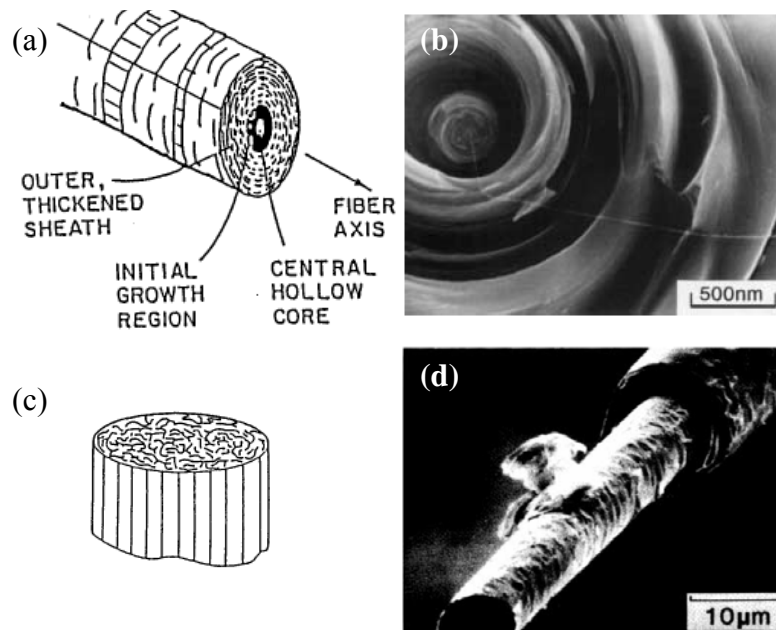


**Figure 2.2.** Structure of carbon nanofibers. (a) Schematic of a carbon nanofiber showing concentrically arranged graphite sheets in the core. (b) TEM image of the concentric graphite sheets. (c) Arrangement of graphite sheets in the nanofiber core is changed from concentric to random after heat treatment to 3000°C. (d) “Sword-in-sheath” failure mode can be observed in this carbon fiber; random arrangement of graphite sheets acts to decrease this mode of failure. From reference [6].

### 2.3. CLAY PARTICLES

Clay particles have a sheet-like crystal structure and are usually in the form of platelets. Their basic structure is composed of silicon–oxygen (silicate) sheets combined with aluminum– or magnesium–oxygen–hydroxyl sheets.<sup>7</sup> Silicon and oxygen atoms are coordinated in a tetrahedron whereas the metal and oxygen and hydroxyls are arranged in octahedrons. Different combinations of the above elements correspond to different types of clays. For example, montmorillonite is an aluminosilicate having two silicate sheets sandwiching an aluminium–oxygen (alumina) sheet (Figure 2.3a), while hectorite consists of two silicate sheets sandwiching a magnesium–oxygen sheet. In dry powdered form,

clay platelets stack up due to weak van der Waals attractions. Clay stacks can be studied using X-ray Diffraction (XRD), from which the periodicity of the stack (also known as the basal or gallery spacing, see Figure 2.3) can be obtained. The gallery spacing of montmorillonite is about 9.6 Å for dry clay and it expands to about 12 Å when the clay is exposed to moisture.

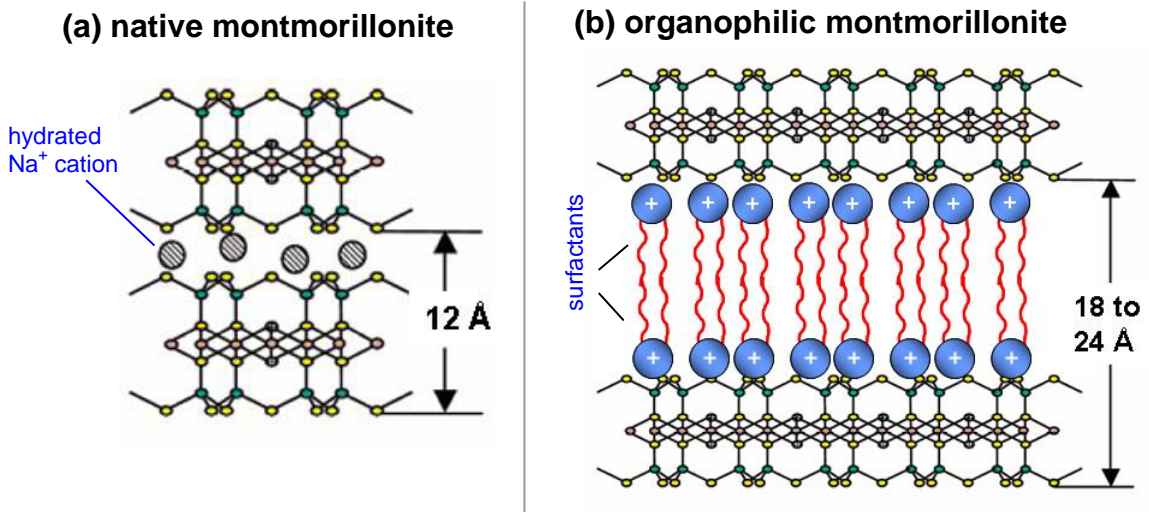


**Figure 2.3.** Schematics of native and organophilic clay. (a) Native montmorillonite showing a stack of two platelets. Each platelet is composed of three sheets, with two silicate sheets sandwiching an alumina sheet. The gallery spacing between the two platelets is about 12 Å. (b) Organophilic montmorillonite, obtained by treating the native clay with a cationic double-tailed surfactant, shown as molecules with a blue head and two red tails. The surfactant replaces the Na<sup>+</sup> cations and its tails are directed outwards from the clay surface. The gallery spacing between the platelets in a stack consequently increases to ca. 20 Å.

Clay particles have a hydrophilic surface and when suspended in water they disperse as individual platelets. In order to make clays compatible with polymers, the particle surface must first be rendered hydrophobic. The procedure to modify the clay surface typically involves the electrostatic binding of a cationic surfactant onto the

negatively charged clay surface.<sup>8</sup> The surfactant headgroup binds onto the clay surface while the hydrophobic surfactant tails point outwards from the clay surface, as shown in Figure 2.3b. This makes the platelets organophilic. In dry powdered form, the organophilic clay platelets still stack up, but they show an increase in gallery spacing to values between 18 and 24 Å, depending on the tail length of the surfactant (Figure 2.3b).

## 2.4. POLYMER NANOCOMPOSITES

The term “polymer nanocomposite” is generally used to refer to a polymeric material filled with particles that have at least one dimension less than 100 nm. Most of the research on polymer nanocomposites have been done with clay fillers. The literature on polymer-clay nanocomposites highlights the importance of particle dispersion on material properties. Depending on the level of dispersion, such nanocomposites may be classified into three different morphologies, as shown schematically in Figure 2.4.<sup>9</sup> The first of these is the *phase separated* morphology, wherein the polymer and clay are completely incompatible with each other. Note that the clay in this case exists as stacks of platelets, typically several microns in size. This would arise if the native hydrophilic clay was used, and in such cases the mechanical properties would be hardly altered by particle addition. The second morphology is the *intercalated* one, wherein polymer molecules diffuse inside the clay stacks, increasing the separation between platelets but preserving stack order. The third morphology is the *exfoliated* or delaminated one, wherein all stack order is lost and the platelets are fully dispersed at the nanoscale in the polymer matrix. Significant improvements in mechanical or rheological properties are found in the case of the intercalated, and especially the exfoliated morphologies.

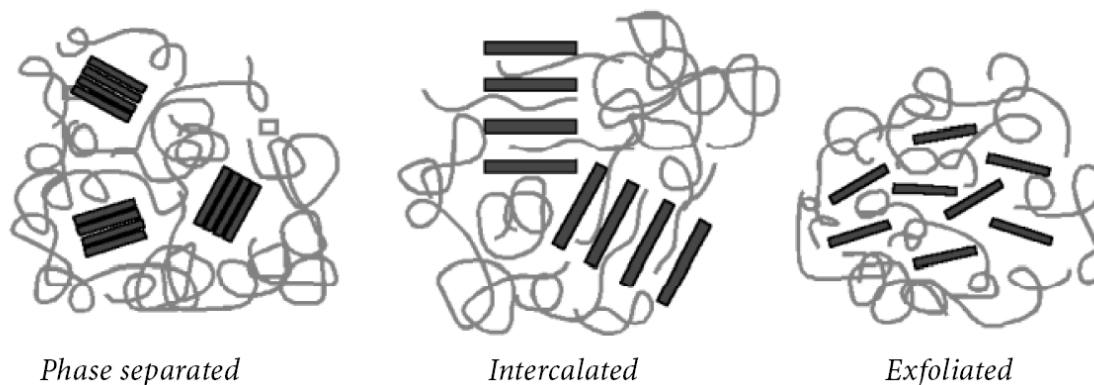


**Figure 2.4.** Schematics of the different morphologies of polymer-clay nanocomposites. From reference [9].

A goal of clay nanocomposite research has been to produce well-dispersed (preferably exfoliated) clay particles in the polymer matrix. The type of morphology can be characterized by XRD and transmission electron microscopy (TEM). Intercalated composites will show an increase in gallery spacing in XRD relative to the gallery spacing of the organophilic clay used. For example, the gallery spacing may increase from ca. 20 Å for the clay powder to ca. 30 Å after polymer intercalation. XRD data on exfoliated composites, on the other hand, will generally not show any crystalline peaks (only a single amorphous peak, characterizing an average distance between the platelets, will be observed).

## 2.5. RHEOLOGICAL PROPERTIES AND THEIR MEASUREMENT

A main focus of this proposal is on the rheological properties of polymer nanocomposites. Rheology is formally defined as the study of flow and deformation in materials.<sup>10</sup> The importance of rheology arises from the fact that rheological parameters

help to correlate the nanoscale morphology to the macroscopic properties. Rheological parameters are typically measured under steady or dynamic oscillatory shear. In steady shear, the sample is subjected to a constant shear-rate  $\dot{\gamma}$  (e.g. by applying a continuous rotation at a fixed rate on a rotational instrument), and the response is measured as a shear-stress  $\sigma$ . The ratio of shear-stress  $\sigma$  to shear-rate  $\dot{\gamma}$  is the (apparent) viscosity  $\eta$ . A plot of the viscosity vs. shear-rate  $\dot{\gamma}$  is called the flow curve of the material.

Rheological experiments can also be conducted in dynamic or oscillatory shear, where a sinusoidal strain  $\gamma = \gamma_0 \sin(\omega t)$  is applied to the sample. Here  $\gamma_0$  is the strain-amplitude (i.e. the maximum applied deformation) and  $\omega$  is the frequency of the oscillations. The sample response will be in the form of a sinusoidal stress  $\sigma = \sigma_0 \sin(\omega t + \delta)$  which will be shifted by a phase angle  $\delta$  with respect to the strain waveform. Using trigonometric identities, the stress waveform can be decomposed into two components, one in-phase with the strain and the other out-of-phase by  $90^\circ$ :

$$\sigma = G' \gamma_0 \sin(\omega t) + G'' \gamma_0 \cos(\omega t) \quad (1)$$

where  $G'$  is the **Elastic** or **Storage Modulus** and  $G''$  is the **Viscous** or **Loss Modulus**. A third parameter, the **complex viscosity**  $\eta^*$  can be calculated from  $G'$  and  $G''$  using the following equation:

$$\eta^* = \frac{\sqrt{G'^2 + G''^2}}{\omega} \quad (2)$$

Note that the **complex viscosity**  $\eta^*$  has the same physical meaning as the steady viscosity  $\eta$ . Indeed, the functions  $\eta^*(\omega)$  and  $\eta(\dot{\gamma})$  have been empirically shown to be identical for

a variety of materials (both the angular frequency  $\omega$  and the shear rate  $\dot{\gamma}$  have the same units, i.e.,  $s^{-1}$ ). This empirical observation is often called the Cox-Merz rule.

The physical interpretations of the elastic and viscous moduli are as follows. The elastic modulus  $G'$  is the in-phase component of the stress and provides information about the elastic nature of the material. Since elastic behavior implies the storage of deformational energy, this parameter is also called the storage modulus. The viscous modulus  $G''$ , on the other hand, is the out-of-phase component of the stress and characterizes the viscous nature of the material. Since viscous deformation results in the dissipation of energy,  $G''$  is also called the loss modulus. For these properties to be meaningful, the dynamic rheological measurements must be conducted within the “*linear viscoelastic*” (LVE) regime of the sample. This means that the stress must be linearly proportional to the imposed strain (i.e., moduli independent of strain amplitude). In that case, the elastic and viscous moduli are only functions of the frequency of oscillations  $\omega$ , and are true material functions. A log-log plot of the moduli vs. frequency, i.e.  $G'(\omega)$  and  $G''(\omega)$ , is called the frequency spectrum or *dynamic mechanical spectrum* of the material. Such a plot represents a signature of the nanoscale morphology of the material.

The important advantage of dynamic shear is that it allows us to characterize microstructures without disrupting them in the process. The net deformation imposed on the sample is minimal because the experiments are restricted to small strain amplitudes within the LVE regime of the sample. As a result, the linear viscoelastic moduli reflect

the microstructures present in the sample at rest. This is to be contrasted with steady shear, where the material functions are always obtained under flow conditions corresponding to relatively drastic deformations. We can therefore correlate dynamic rheological parameters to static microstructures, and parameters under steady shear to flow-induced changes in microstructure.

## **2.6. FLAMMABILITY PROPERTIES AND THEIR MEASUREMENT**

As mentioned in Chapter 1, polymers are extremely useful materials yet they suffer from being inherently flammable. However, it has been found that the addition of anisotropic nanoscale fillers results in lowering of the flammability while enhancing other polymer properties. To study the flammability properties of the resulting composites, we used a cone calorimeter built by NIST. The cone calorimeter is one of the most effective bench-scale methods for studying the flammability properties of materials.

<sup>11</sup> Fire-relevant properties, measured by the cone calorimeter, such as heat release rate (HRR), *peak* HRR, and smoke and carbon monoxide yield, are vital to the evaluation of the fire safety of materials. The ignition characteristics, heat release rate, and sample mass loss rate according to ASME E1354/ISO 5660. An external radiant heat flux of 50 kW/m<sup>2</sup> was applied. All of the samples were measured in the horizontal position and wrapped with a thin aluminum foil except for the irradiated sample surface. The standard uncertainty of the measured heat release rate was  $\pm 10\%$ .

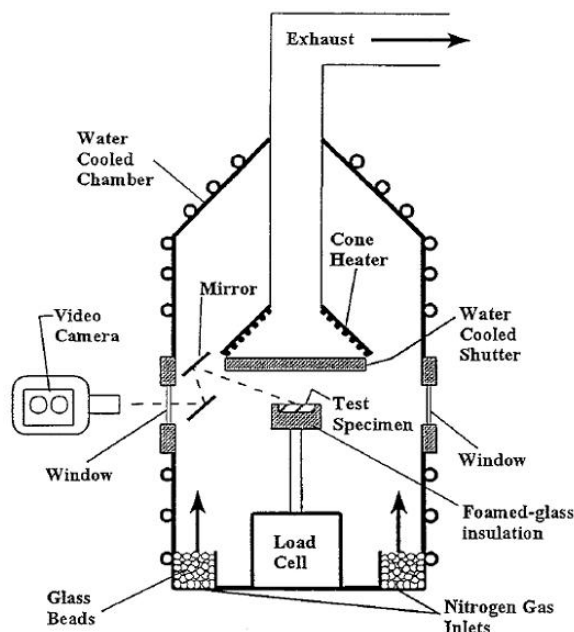


**Figure 2.5.** Schematic of the radiant gasification apparatus constructed at NIST to study the condensed phase processes during burning. From reference [12].

We also employed a radiant gasification apparatus, somewhat similar to a cone calorimeter, which was designed and constructed at NIST to study the gasification processes of samples by measuring mass loss rate and temperatures of the sample exposed to a fire-like heat flux in a nitrogen atmosphere (no burning). A schematic of the gasification apparatus is shown in Figure 2.5. The apparatus consists of a stainless-steel cylindrical chamber that is 1.70 m tall and 0.61 m in diameter. In order to maintain a negligible background heat flux, the interior walls of the chamber are painted black and the chamber walls are water-cooled to 25 °C. All experiments were conducted at 50 kW/m<sup>2</sup>. The unique nature of this device is threefold: (1) observation and results obtained from it are only based on the condensed phase processes due to the absence of any gas phase oxidation reactions and processes; (2) it enables visual observations of gasification

behavior of a sample using a video camera under a radiant flux similar to that of a fire without any interference from a flame; (3) the external flux to the sample surface is well-defined and nearly constant over the duration of an entire experiment (and over the spatial extent of the sample surface) due to the absence of heat feedback from a flame. A more detailed discussion of the apparatus is given in our previous study;<sup>12</sup> the standard relative uncertainty of the measured mass loss rate is  $\pm 10\%$ .

## 2.7. ELECTRICAL CONDUCTIVITY AND ITS MEASUREMENT

Electrical conductivity is one of the most sought after properties of polymer nanocomposites.<sup>13</sup> An advantage of anisotropic electrically conductive fillers is that the corresponding percolation thresholds are lower than for isotropic fillers. In fact, extremely low percolation thresholds have been reported in the case of SWNTs and MWNTs compared to carbon black. The electrical conductivity is obtained from measurements of resistance as follows:

$$\sigma = \frac{1}{\rho} = \frac{t}{\Omega * A}$$

In this equation,  $\sigma$  is the electrical conductivity,  $\rho$  is the resistivity,  $\Omega$  is the resistance,  $t$  is the thickness and  $A$  is the area. It is worth distinguishing  $\rho$  from  $\Omega$ ; whereas  $\rho$  is a bulk material property,  $\Omega$  is geometry dependent. In this study, the electrical conductivity of the composites was measured in accordance with ASTM D4496. Samples of a known cross-sectional area and thickness were placed between copper electrodes and the DC resistance was measured using a Fluke 87 multimeter. The surfaces of the sample in contact with the electrodes were coated with silver paint in order to reduce discrepancies

arising from micro-roughness. It was ensured that the surface area of the electrodes exceeded the cross-sectional area of the discs.

# Chapter 3

## EFFECT OF ASPECT RATIO OF MWNTs ON NANOCOMPOSITE PROPERTIES

The results presented in this chapter have been published in the following journal article:  
Bani H. Cipiriano, Takashi Kashiwagi, Srinivasa R. Raghavan, Ying Yang, Eric A. Grulke, Kazuya Yamamoto, John R. Shields and Jack F. Douglas, “*Effects of Aspect Ratio of Multi-Walled Carbon Nanotubes on the Flammability Properties of Polymer Nanocomposites.*” *Polymer* **48** (2007) [doi:10.1016/j.polymer.2007.07.070](https://doi.org/10.1016/j.polymer.2007.07.070)

### 3.1. INTRODUCTION

Polymer nanocomposites have attracted a great deal of interest due to their ability to improve physical properties of polymers such as mechanical and thermal properties. In particular, polymer-carbon nanotube nanocomposites have been extensively studied to explore their unique electronic, thermal, optical, and mechanical properties,<sup>14-18</sup> as summarized in recent review articles.<sup>19,20</sup> Furthermore, an improvement in the flammability properties of polymers has been achieved with polymer-carbon nanotube nanocomposites, which could provide an alternative to conventional flame retardants.<sup>3,21-27</sup> The outstanding improvement of physical properties with carbon nanotubes is in part attributed to their extremely high aspect ratio (length-to-outer diameter ratio) of up to 1000. Increasing the aspect ratio of single-walled carbon nanotubes (SWNT) resulted in an increase in the Young’s modulus<sup>28</sup> and a reduction in the critical concentration required for the formation of a percolation network.<sup>29</sup> In addition, by employing large

aspect ratio nanotubes, higher electrical and thermal conductivities were achieved in epoxy-carbon nanotube nanocomposites<sup>30</sup> as well as higher thermal conductivities in poly  $\alpha$ -olefin/multi-walled carbon nanotube nano-composites.<sup>31</sup> Furthermore, improvements in the gas barrier<sup>32,33</sup> and mechanical properties<sup>34-36</sup> of polymer-clay nanocomposites by using larger aspect ratios (length-to-thickness ratio) of clay particles were reported.

Although many studies have shown the enhancement of physical properties of polymer nanocomposites by using larger aspect ratio carbon nanotubes and clay particles as described above, only a limited study of the effects of nanoparticle aspect ratio on the flammability properties of polymer nanocomposites has been reported. In particular, the measurement has been limited to clay nanocomposites.<sup>37</sup> Since we are not aware of any study with carbon nanotubes, the objective of this study is to determine the effects of aspect ratio of MWNT on the flammability properties of polystyrene (PS). In a previous study, it has been demonstrated that the formation of a jammed network of carbon nanotubes in the nanocomposites is critically required to significantly reduce the heat release rate of the nanocomposites.<sup>3</sup> Therefore, we will test the ability of MWNTs of varying aspect ratios to form jammed networks in the nanocomposites through dynamic rheology measurements of the storage modulus at elevated temperatures. Then we will draw comparisons between the expected flammability performance based on the rheology data and the actual behavior observed in flammability experiments.

### 3.2. EXPERIMENTAL

**Materials.** The matrix polymer used in this study was PS (Styron 666D, Dow Chemical, melt mass flow rate of 8.0 g/10 min at 200 °C). Two different MWNTs were used; one was purchased from Hyperion Catalyst International as a form of master batch with a mass concentration of 20% in PS. Other MWNTs were made using xylene as a carbon source and ferrocene as a catalyst at about 675 °C by a, chemical vapor deposition, CVD, method at the University of Kentucky.<sup>38</sup>

**Composites.** Composites were prepared by melt blending the MWNT-polystyrene mixture in a Haake PolyLab shear mixer. The mixture temperature was set at 180 °C and the polystyrene pellets were added to the mixer running at a speed of 20 rpm. The pellets melted in about 3 min, and the MWNTs were added at this time; the mixing was continued for 40 min. For the Hyperion master batch, appropriate amounts of the PS pellets and of the master batch pellets were mixed and fed into a B & P Process Equipment twin-screw extruder (co-rotating, intermeshing, L:D equals 25:1). Operating conditions were 400 rpm screw speed and 185 °C barrel temperature in all zones except the last zone (195 °C). Samples with mass concentrations of 0.2 %, 0.5 %, 1%, 2%, and 4% MWNT were prepared with the two MWNTs. All samples for measuring flammability properties (discs of 75 mm diameter and 4 mm thick) were compression molded at 200 °C under a pressure of about 1.4 MPa for a duration of 15 minutes.

**Confocal Microscopy.** The morphologies of the nanotubes in the melt blended samples were evaluated using a laser confocal microscope (Model LSM510, Carl Zeiss Inc.) to

image the MWNTs in the PS matrix. The confocal microscope utilizes coherent laser light and collects reflected light exclusively from a single plane with a thickness of 100 nm (a pinhole sits conjugated to the focal plane and rejects light out of the focal plane). A red laser ( $\lambda = 633$  nm) was used as the coherent light and images were taken at 100 x magnification with an Epiplan-Neofluar 100 x/1.30 oil-pool objective. An LP385 (Rapp Opto Electronic) filter was used to limit the lower spectra of reflected light. One hundred two-dimensional images (optical slices with 512 pixels x 512 pixels), with scan size 92.1 x 92.1  $\mu\text{m}$ , were taken at a spacing of 100 nm by moving the focal plane.

**TEM and SEM.** The aspect ratio of the MWNTs was evaluated using scanning and transmission electron microscopy (SEM and TEM). The SEM, Phillips ESEM-E3, was operated at a voltage of 30 kV. The TEM, Hitachi H-600, was operated at a voltage of 100 kV. MWNTs were isolated from the nanocomposite by extraction of polystyrene in tetrahydrofuran, THF. The MWNTs were then dried and redispersed at very low concentrations ( $\sim 0.01$  mg/mL) in THF by stirring. Ultrasonication was avoided since it is known to modify nanotube length. Drops of the MWNT dispersion in THF were dried onto freshly cleaved mica surfaces for evaluation using SEM. Nitrogen was blown on the drops to vaporize the THF quickly and prevent substantial tube aggregation. For evaluation using TEM, drops of the dispersion were dried onto a copper grid covered with carbon film (Ted Pella, Redding, CA).

**Rheological Studies.** Rheological experiments were performed on an RDAIII strain-controlled rheometer (TA Instruments) equipped with a convection oven. A parallel plate

geometry (25 mm diameter) was used with a gap of 0.9 mm. Samples were prepared by melt-pressing nanocomposite pellets at 150°C and a pressure of about 0.93 MPa. All rheological experiments were performed at 200°C and in a nitrogen atmosphere to avoid oxidative degradation of polystyrene. The gap reference was set at 200°C. Dynamic rheological experiments were conducted to measure the storage and loss moduli as a function of frequency (0.01 to 100 rad/s) at a constant strain of 0.5% (this value of strain was verified to be in the linear viscoelastic regime of the sample). Thermogravimetric analysis (TGA) was conducted using a TA Instruments TGA Q500 at 5°C/min from 90°C to 500°C in nitrogen (flow rate of 60 cm<sup>3</sup>/min) for the original nanocomposite samples (about 5 mg) in a platinum pan.

**Flammability Studies.** A cone calorimeter built by NIST was used to measure ignition characteristics, heat release rate, and sample mass loss rate according to ASME E1354/ISO 5660. An external radiant heat flux of 50 kW/m<sup>2</sup> was applied. All of the samples were measured in the horizontal position and wrapped with a thin aluminum foil except for the irradiated sample surface. The standard uncertainty of the measured heat release rate was ± 10 %. A radiant gasification apparatus, somewhat similar to a cone calorimeter, was designed and constructed at NIST to study the gasification processes of samples by measuring mass loss rate and temperatures of the sample exposed to a fire-like heat flux in a nitrogen atmosphere (no burning). The apparatus consists of a stainless-steel cylindrical chamber that is 1.70 m tall and 0.61 m in diameter. In order to maintain a negligible background heat flux, the interior walls of the chamber are painted black and the chamber walls are water-cooled to 25 °C. All experiments were conducted

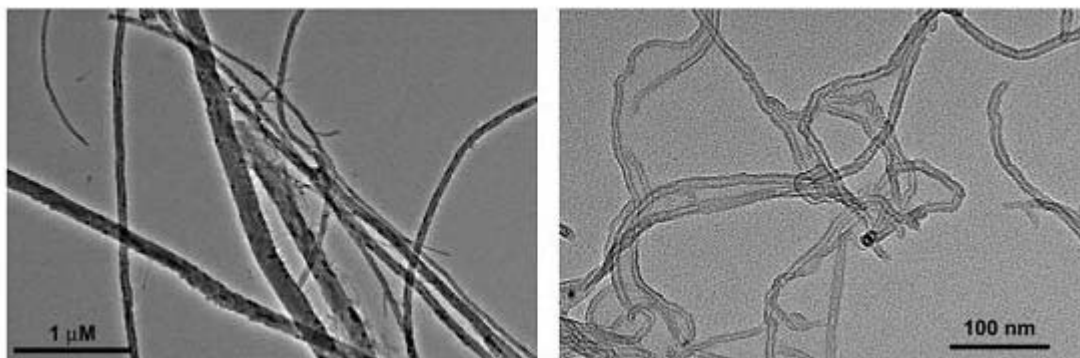
at 50 kW/m<sup>2</sup>. The unique nature of this device is threefold: (1) observation and results obtained from it are only based on the condensed phase processes due to the absence of any gas phase oxidation reactions and processes; (2) it enables visual observations of gasification behavior of a sample using a video camera under a radiant flux similar to that of a fire without any interference from a flame; (3) the external flux to the sample surface is well-defined and nearly constant over the duration of an entire experiment (and over the spatial extent of the sample surface) due to the absence of heat feedback from a flame. A more detailed discussion of the apparatus is given in our previous study;<sup>12</sup> the standard relative uncertainty of the measured mass loss rate is  $\pm 10\%$ .

### **3.3. RESULTS**

#### **3.3.1. Aspect Ratio and Morphology of the MWNTs in PS**

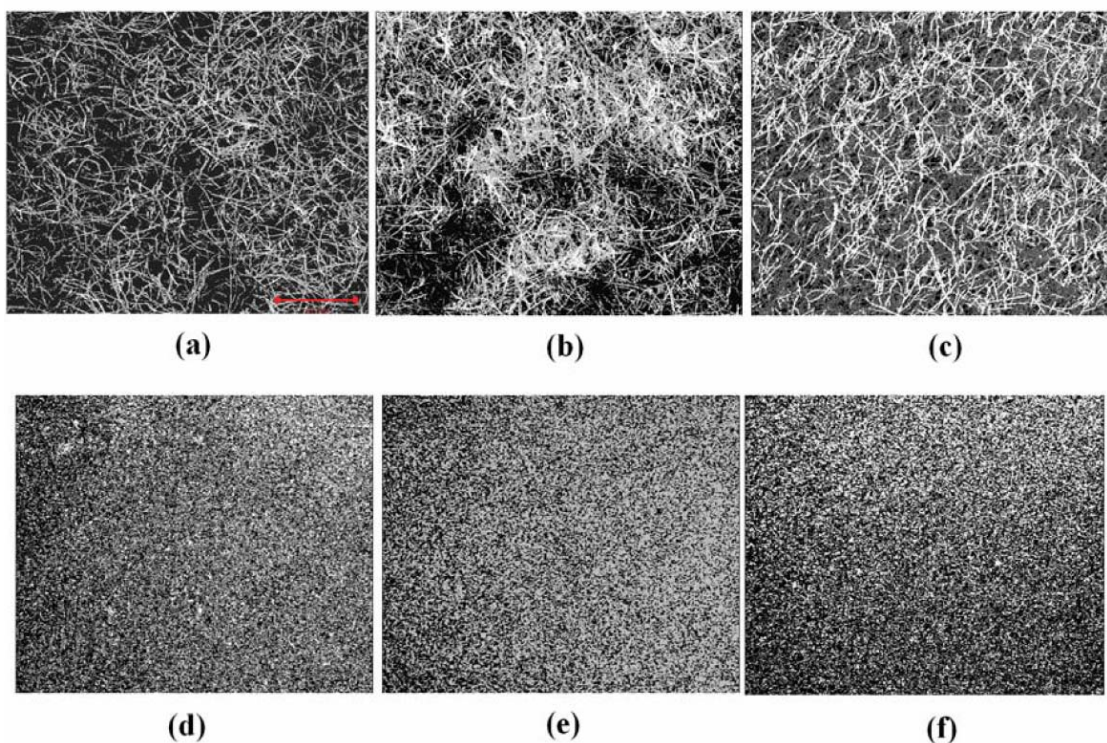
TEM images of the two types of MWNTs studied here (from Kentucky and Hyperion, respectively) are shown in Figure 3.1. In order to determine the aspect ratio for both types of MWNTs, it is important to extract the MWNTs from compounded PS-MWNT samples because particle sizes might be modified during extrusion. A minimum of 140 measurements of diameter and of 200 measurements of length were conducted for both types of MWNTs. The average diameter and length of the Kentucky MWNTs were obtained by SEM (images not shown) and they are  $75 \pm 54$  nm and  $11.3 \pm 5.6$   $\mu$ m, respectively. The dimensions of the Hyperion MWNTs were determined by using TEM and they are  $7.1 \pm 2.5$  nm and  $351 \pm 195$  nm, respectively. The large standard deviation was mainly due to a few large or extremely long and large tubes (histograms not shown). The average aspect ratio obtained by dividing the average length by the average diameter

is 150 for the Kentucky MWNTs and 49 for the Hyperion MWNTs. Henceforth, the Kentucky MWNTs will be designated as MWNT-150 and the Hyperion MWNTs as MWNT-49.



**Figure 3.1.** TEM images of the MWNTs extracted from the composites, left is MWNTs in the PS/MWNT prepared at University of Kentucky and right is MWNTs in the PS/MWNT compounded with the Hyperion master batch.

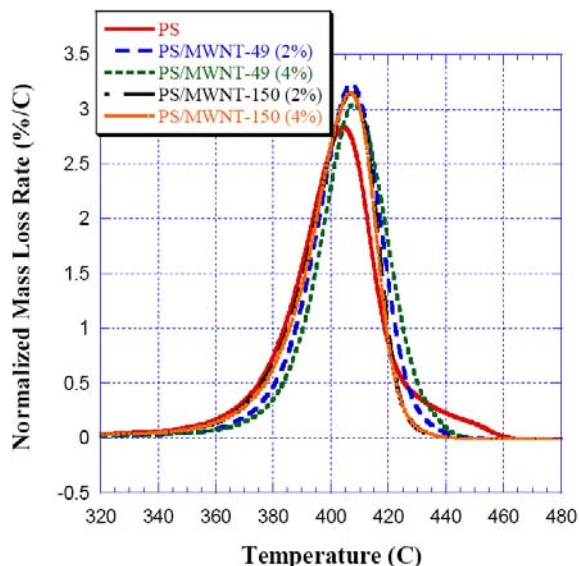
Since a good dispersion of the nanotubes in the polymer matrix is crucial for the reduction in flammability,<sup>27,39</sup> the distribution of the tubes in the PS/MWNT samples was examined by confocal microscopy, as shown in Figure 3.2. Each MWNT-150 tube can be seen in the figure and these tubes are well dispersed in PS without forming many agglomerates. However, confocal microscopy does not possess enough spatial resolution to distinguish individual MWNT-49 tubes due to their much smaller size than MWNT-150. All images show no formation of agglomerates except some possibility in the image of Figure 3.2(b). From these images and others (not shown), we consider that both tubes were reasonably well-dispersed in PS.



**Figure 3.2.** Confocal microscopy images with a scale bar of 20  $\mu\text{m}$  : (a) PS/MWNT-150 (1%), (b) PS/MWNT-150 (2%), (c) PS/MWNT-150 (4%), (d) PS/MWNT-49 (1%), (e) PS/MWNT-49 (2%), (f) PS/MWNT-49 (4%).

### 3.3.2. Thermal Stability

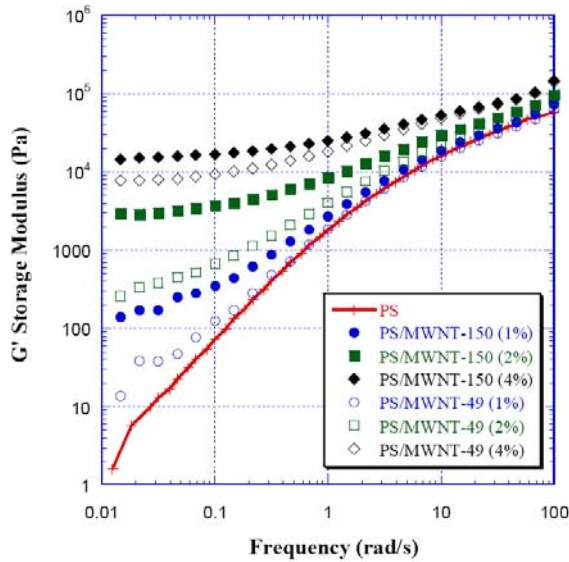
Thermogravimetric analysis was conducted in nitrogen at a heating rate of 5  $^{\circ}\text{C}/\text{min}$ . Although previous studies did not conclusively exclude the effects of oxygen in surrounding air on thermal degradation of polymeric materials during burning of polymers, oxidation reactions of the polymers appear to be insignificant (oxygen is mainly consumed by gas phase reactions i.e., the flame). An exception is the case in which the flame does not cover the entire burning surface or the burning/pyrolysis rate is extremely low.<sup>40,41</sup> As shown in Figure 3.3, the thermogravimetric analysis results indicate that the thermal stability of PS is unaffected either by the addition of MWNT-150 or of MWNT-49 at all loadings studied.



**Figure 3.3.** Derivative thermogravimetric mass loss rates of selected samples.

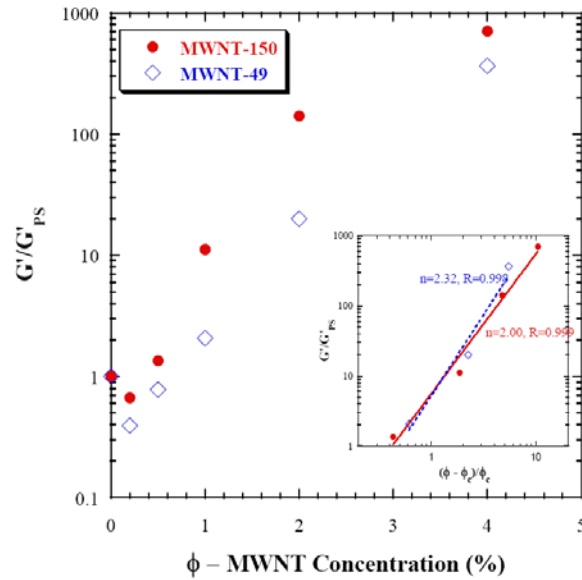
### 3.3.3. Viscoelastic Properties

We previously found that nanocomposites based on carbon nanotubes are capable of forming a continuous network-structured protective layer that mainly consists of the tubes and is free from any opening or cracks.<sup>3,27</sup> (Vigorous bubbling through any opening or cracks supplies combustible degradation products to a flame, which compromises the flame retardant effectiveness). This results in a significant reduction in heat release rate (a flammability measure related to the intensity/size of fire; the lower the heat release rate smaller the size of fire) and in the case of carbon nanotubes, the protective layer was formed at a mass concentration of as low as 0.5 %.<sup>3</sup> Since the jammed network that gives rise to the protective layer is formed in the initial composite samples, flame retardant effectiveness can be predicted by measurement of the storage modulus of these samples. The storage modulus  $G'$  provides a measure of the nanocomposites' stiffness, and its frequency dependence characterizes whether the material is liquid-like or solid-like.



**Figure 3.4.** Effects of aspect ratio and of mass concentration of MWNT on storage modulus of PS/MWNT nanocomposites at 200 °C.

Figure 3.4 plots  $G'$  for PS-MWNT composites made from the MWNTs of two different aspect ratios. At 200°C, the  $G'$  curve of PS shows the typical response of a viscous liquid with  $G' \sim \omega^2$  at low frequencies  $\omega$ . At a 1% MWNT loading, the  $G'$  of the PS/MWNT-49 is slightly higher than that of PS, while the  $G'$  of PS/MWNT-150 is even higher. At higher mass concentrations of MWNTs, the liquid-like low-frequency scaling of  $G'$  disappears and  $G'$  becomes nearly constant at low frequencies. We term the composition at which this rheological state is achieved as the ‘gel concentration’,  $\phi_g$ . We define  $\phi_g$  as the concentration at which  $G'$  becomes independent of  $\phi$  for an extended low-frequency range. The  $\phi_g$  of the composites with MWNT-150 is between 1–2 % compared to about 4% with MWNT-49.



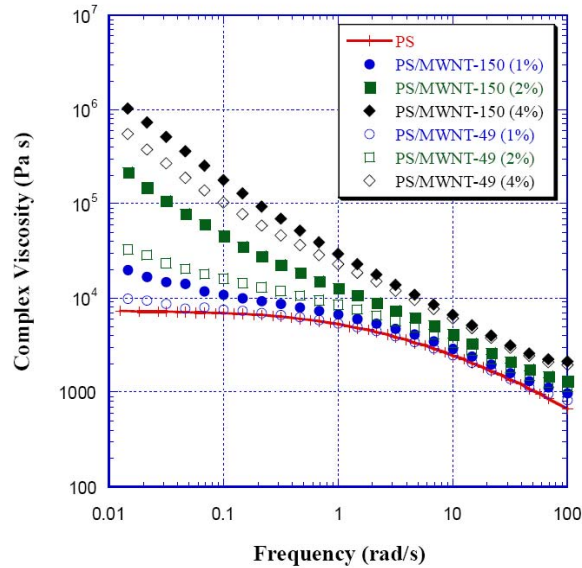
**Figure 3.5.** The relationship between mass concentration of MWNT and normalized storage modulus of PS/MWNT nanocomposites at a frequency of 0.05 rad/s and 200 °C with that of PS. Insert is the power law relationship between the normalized storage modulus and normalized mass concentration of MWNT with percolation mass concentration  $P_c$ .

Figure 3.5 plots the storage modulus measured at a frequency of 0.5 rad/s for PS/MWNT-150 and PS/MWNT-49 as a function of MWNT concentration. This data reiterates that the  $G'$  for MWNT-150 composites is significantly larger than that for MWNT-49 at all mass concentrations studied. Note that at a mass concentration of 0.1% with MWNT-150 and 0.1 and 0.2% with MWNT-49 the  $G'$  of the composites are less than that of pristine PS. This reduction in  $G'$  is due to a small reduction in molecular weight of PS during compounding, and similar reduction in  $G'$  has been observed for extruded polymer-clay composites at low clay concentrations.<sup>42,43</sup>) If we define a percolation concentration of MWNT,  $\phi_c$ , as the concentration when the intertube interactions dominate over polymer chain interactions,  $\phi_c$  for PS/MWNT-150 is about 0.35% and that for PS/MWNT-49 is 0.62 %. It has been known that a bulk ‘stiffness’  $G'$

of the composites varies phenomenologically with mass concentration according to a power law<sup>29,44</sup>

$$G'/G'_{PS} \sim [(\varphi - \varphi_c)/\varphi_c]^\beta$$

The insert in Figure 3.5 shows that the above relationship adequately describes the  $G'$  data for both PS/MWNT-150 and PS/MWNT-49, with the value of  $\beta = 2$  for the former and 2.3 for the latter. Indeed, a  $\beta = 2$  is a typical experimental value for networks of stiff fibers.<sup>45</sup>



**Figure 3.6.** Effects of aspect ratio and of mass concentration of MWNT on complex viscosity of PS/MWNT nanocomposites at 200 °C.

We now consider the effects of MWNT aspect ratio and concentration on the complex viscosity of PS/MWNT samples at 200 °C (Figure 3.6). Since suppression of bubbling caused by the nucleation of degradation products in the polymer melt<sup>46</sup> is required for effective flame retardant performance, the melt viscosity of the composites at elevated temperatures might play an important role in this process. The data in Figure 3.6

shows an increase by about two orders of magnitude in the complex viscosity at low frequencies upon addition of 4% MWNTs. This significant increase in complex viscosity indicates an increasing importance of tube-tube interactions in dictating the rheological response.<sup>45,47</sup> Figure 3.6 also shows that the complex viscosities of the composites with MWNT-150 are higher than those with MWNT-49 at the same mass concentration (similar to the trend in Figures 3.4 and 3.5 for  $G'$ ). These results suggest that the PS/MWNT-150 samples should be less flammable than those of PS/MWNT-49 at the same MWNT concentration.

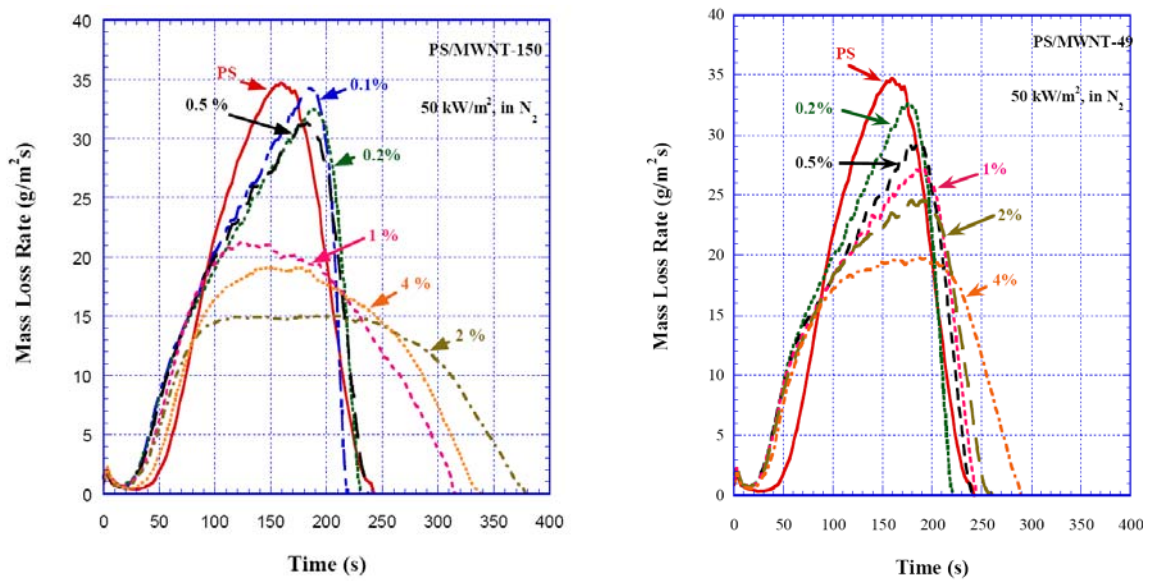


**Figure 3.7.** Effects of mass concentration of MWNT on mass loss rate of PS/MWNT nanocomposites at 50 kW/m<sup>2</sup> in nitrogen. (a) Samples with MWNT-150 and (b) with MWNT-49.

### 3.3.4. Flammability Properties

The mass of a sample was continuously measured when exposed to an external radiant flux of 50 kW/m<sup>2</sup> in a slow flowing nitrogen atmosphere and the mass loss rate

was calculated by taking the time derivative of the measured weight change. The results with PS/MWNT-150 and with PS/MWNT-49 at various mass concentrations of the MWNT are shown in Figure 3.7 (a) and Figure 3.7 (b), respectively. PS behaved like a liquid with numerous bubbles during the test and no char was left in the container. Similarly, samples with low mass concentrations of both types of MWNTs behaved like a viscous liquid with accompanying formation and bursting of many large bubbles and formation of many small black islands. Such islands were left at the end of the test and their pictures are shown in Figure 3.8. The number and size of the islands increased with an increase in mass concentration of the two MWNTs. At these low mass concentrations, nanocomposites prepared from both types of MWNTs exhibited a relatively small reduction in mass loss rate. In contrast, with 1% of MWNT-150, the sample behaved almost like a solid with a wavy surface contour and PS/MWNT-150 (2%) and PS/MWNT-150 (4%) both behaved like solids by forming a uniform protective layer with a smooth surface without any openings. This layer has a randomly interlaced network structure mainly consisting of the MWNTs.<sup>23,27</sup> PS/MWNT-150 (2%) has the lowest mass loss rate as shown in Figure 3.9. However, PS/MWNT-150 (4%) has higher peak mass loss rate than that of PS/MWNT-150 (2%). This is probably due to an increase in thermal conductivity of the sample at high MWNT mass concentration which tends to slow the increase in initial mass loss rate but to increase it later after accumulation of energy in the sample.<sup>23</sup> The mass loss rate of PS/MWNT-49 decreases with an increase in mass concentration of the tubes but the peak mass loss rate tends to be higher than that of PS/MWNT-150 at the same mass concentration of tubes. It appears that true percolation-like behavior is not responsible for the reduction in mass loss rate of PS/MWNT-49. The

residue even at 4 % mass concentration consisted of numerous granular, coarse particles, as shown in Figure 3.8, instead of a uniform protective layer. Bubbling in the space between the particles could be seen during the test.

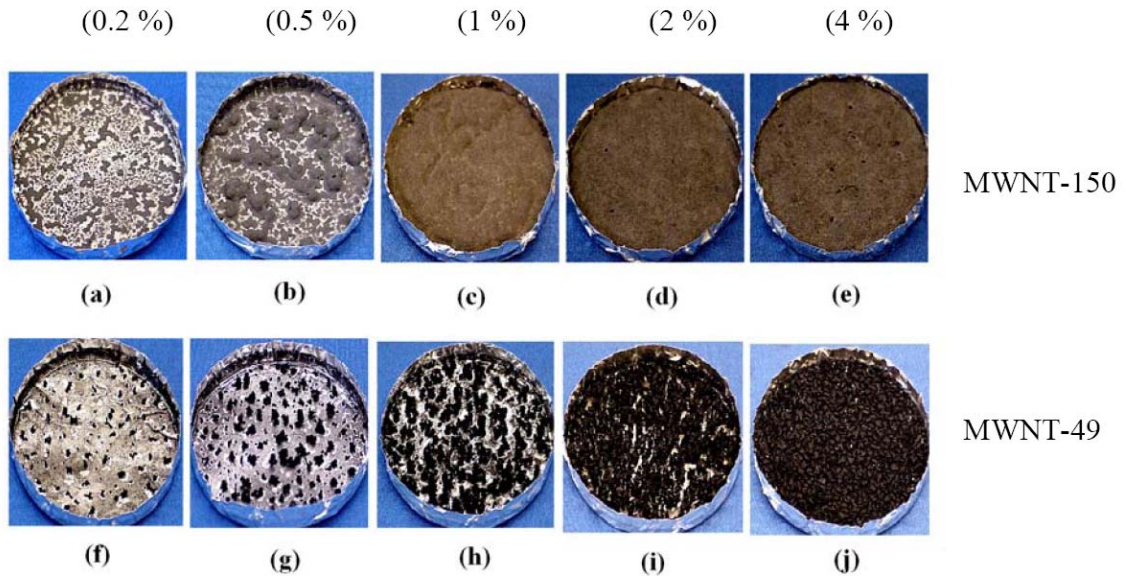


**Figure 3.8.** Comparison of residues of PS/MWNT nanocomposites, based on MWNT-150 and MWNT-49, collected after the gasification test at 50 kW/m<sup>2</sup> in nitrogen.

It has been demonstrated that the flame retardant performance of polymer-carbon nanotube nanocomposites is mainly due to the physical process of heat shielding by the formation of a network-structured protective layer in the condensed phase.<sup>3,23,27</sup> Therefore, it is expected that heat release rate curves of these samples would be similar to the mass loss rate curves shown in Figures 3.7. Observed heat release rate curves with the two different MWNTs at various mass concentrations of the tubes are shown in Figure 3.10. The observed trends are very similar to those observed in Figures 3.7, including lower peak heat release rates for PS/MWNT-150 as compared to those of PS/MWNT-49

at the same tube mass concentration. Furthermore, the peak heat release rate of PS/MWNT-150(4%) is higher than that of PS/MWNT150(2%) as observed in Figure 3.10 due to an increase in thermal conductivity for PS/MWNT-150(4%) as described above.

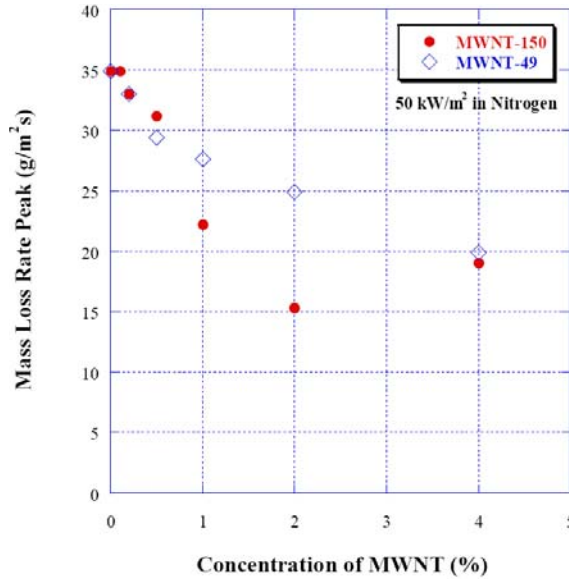


**Figure 3.9.** The effects of aspect ratio of MWNT on the relationship between mass loss rate peak and mass concentration of MWNT.

### 3.4. DISCUSSION

The above results clearly show the dependence of both the viscoelastic and flammability properties of PS/MWNT nanocomposites on the aspect ratio of MWNTs. Since the sizes of the two MWNTs are quite different, it is interesting to explore the significant effects of the aspect ratio. We estimate the difference in the total number of MWNTs in PS/MWNT-150 (average length of 11  $\mu\text{m}$  and average outer diameter of 97 nm) and PS/MWNT-49 (average length of 347 nm and average diameter of 7.1 nm) at the same mass concentration of MWNT. With the assumptions that the outer diameter is

much larger than the inner diameter of both tubes and that both the densities of the two MWNTs are the same, the total number of MWNT-49 is roughly 6,000 times more than that of MWNT-150 in the same volume of the PS/MWNT. Furthermore, the total outer surface area of MWNT-49 in the PS/MWNT-49 is about 14 times greater than that of MWNT-150 in the PS/MWNT-150. However, the results show that the effects of aspect ratio of MWNT are more dominant than the total number of nanotubes or their total surface area. Then, if two MWNT types have the same outer diameter and different aspect ratios (different lengths of tube), it is possible that the effects of aspect ratio on flammability properties might be larger than those observed in this study.

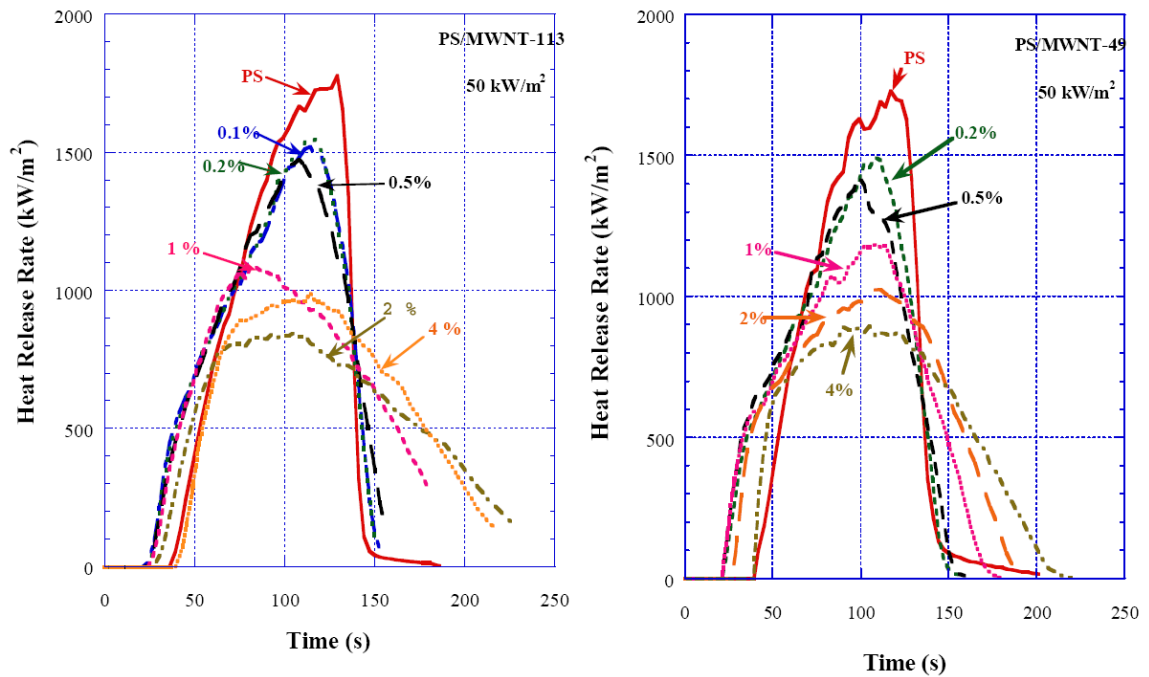


**Figure 3.10.** Heat release rate curves of PS/MWNT nanocomposites at various mass concentrations of MWNT at  $50 \text{ kW/m}^2$ . (a) with MWNT-150 and (b) with MWNT-49.

The importance of aspect ratio of nanoparticles on the formation of the network structured layer and flammability properties were also demonstrated in our previous

study with plate shaped nanoparticles of clay.<sup>37</sup> In that study three different types of clays were used in polypropylene/polypropylene-g-maleic anhydride (PP/PPgMA): synthetic mica (aspect ratio of about 1,200<sup>48</sup>), montmorillonite (MMT) (about 200<sup>48</sup>) and synthetic hectorite (about 50<sup>48</sup>). The sample was a 10 cm x 10 cm x 0.3 cm thick plate and it was tested in nitrogen at 50 kW/m<sup>2</sup>. The lowest mass loss rate was observed for the sample with synthetic mica, which generated a significantly lower mass loss rate than with MMT and synthetic hectorite, as shown in Figure 3.11. The figure shows pictures of the residues of the four samples collected after the tests. The surface of the residue of the sample with synthetic mica is relatively smooth without any large cracks. However, the two samples with the other two clays show large cracks (in particular, with synthetic hectorite). Melting and vigorous bubbling were observed in the cracks during the test. It has demonstrated that the addition of carbon nanotubes or clay having a large aspect ratio into polymers tends to generate residues having a smooth surface without any openings/cracks and to reduce significantly the flammability properties of the polymers.

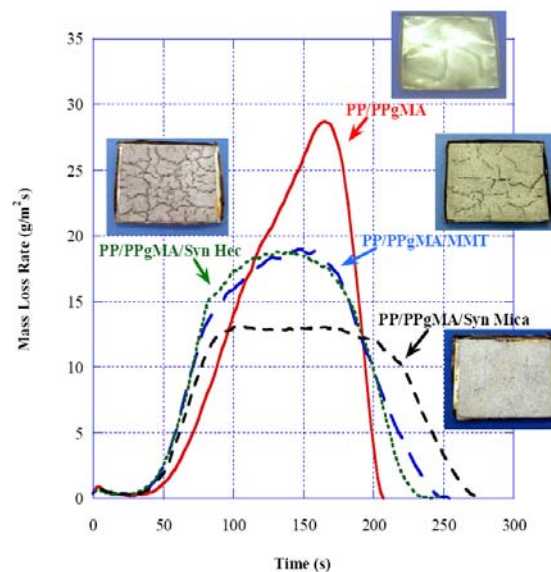


**Figure 3.11.** Effects of clay type on mass loss rate of PP(92.3%)/PPgMA(7.7%) and PP(84.6%)/PPgMA(7.7%)/clay(7.7%) samples in nitrogen at 50 kW/m<sup>2</sup>.

In Figure 3.4, the storage modulus  $G'$  of PS/MWNT-49(4%) is seen to be nearly independent of frequency at low frequencies, which indicates the formation of network structure and such nanocomposite samples having a relatively high complex viscosity formed a protective heat shield layer covering the sample surface without any cracks.<sup>3,23,25</sup> However, it appears that the residue of PS/MWNT-49(4%) collected after the gasification test in nitrogen at 50 kW/m<sup>2</sup> is made of a collection of numerous discrete agglomerates, as shown in Figure 3.8j. Vigorous bubbling was observed around the agglomerates during the test and the mass loss rate of this sample is not as low as that of PS/MWNT-150 (2%) which did form a smooth, network-structured protective layer, as shown in Figure 3.8d. In our previous study, the formation of the network-structured protective layer was observed with poly(methyl methacrylate)/single-walled carbon nanotube (PMMA/SWNT) nanocomposite at a mass concentration of 0.5 %.<sup>3</sup> The aspect ratio of the bundled SWNT was about 45 based on the average diameter of about 7 nm and average length of 310 nm. Since these SWNT bundles and MWNT-49 are about the same size, the size of MWNT-49 is not the reason why PS/MWNT-49 does not form the protective layer. If the dispersion of MWNT-49 in PS/MWNT-49(4 %) were much worse than that of MWNT-150 in PS/MWNT-150 (This does not appear in Figure 4), then the poor dispersion should be reflected in decreased properties of the sample. However, the storage modulus of PS/MWNT-49(4 %) is large and independent of frequency at low frequencies as shown in Figure 3.4. At present, it is not clear why a fully effective protective layer was not formed in the case of PS/MWNT-49.

### 3.5. CONCLUSIONS

The effects of the aspect ratio of MWNT on viscoelastic properties and flammability properties of PS/MWNT nanocomposites were studied with two different MWNTs in the mass concentration from 0.1 % to 4 %. The samples were prepared using twin screw extruders. The average aspect ratios of the two MWNTs, 49 and 150, were determined by analyzing the images of the tubes extracted from the compounded nanocomposites, which were taken by SEM and TEM. No significant effects of aspect ratio on thermal stability of PS/MWNT nanocomposites were observed. However, storage modulus and complex viscosity of PS/MWNT-150 are larger than those of PS/MWNT-49 at the same mass concentration of MWNT. PS/MWNT-150 samples with 2 % and 4 % mass concentration of MWNT-150 form solid-like network structures but only PS/MWNT-49 (4 %) forms this structure. The mass loss rate of PS is more reduced with PS/MWNT-150 and the lowest mass loss rate is observed with PS/MWNT-150(2 %). Slightly higher mass loss rate of PS/MWNT-150(4 %) is probably due to an increase in thermal conductivity. With increasing concentration of MWNT-150, the residue of PS/MWNT-150 changes from the formation of discrete islands to a smooth surface layer without any openings, which is generated at concentrations of 2 % and 4 %. All PS/MWNT-49 samples used in this study did not generate such residues. These results show that the addition of MWNT with large aspect ratios reduces significantly flammability of polymers.

# Chapter 4

## RECOVERY OF NANOCOMPOSITE PROPERTIES BY ANNEALING

### 4.1. INTRODUCTION

Electrically conductive nanoparticles, such as multi-walled carbon nanotubes (MWNTs) and carbon nanofibers (CNFs), have enjoyed immense attention over the last several years. These particles have been of great interest to polymer scientists because their inclusion into polymer matrices gives rise to conductive thermoplastics.<sup>13,20</sup> Indeed, the combination of high conductivity from the particles with the flexibility and easy processability of polymers is a highly desirable mixture. Materials with such unique properties are likely to enable new applications, such as lightweight radiation shields for use by NASA in outer space.<sup>16,49,50</sup> Accordingly, many groups have investigated polymer-MWNT and polymer-CNF nanocomposites, and impressive conductivities have been reported. For example, conductivities around 1 S/m have been realized with loadings of just ca. 2 wt.% of MWNTs<sup>51,52</sup> or 5 wt.% of CNFs.<sup>53</sup>

The polymer-MWNT/CNF composites studied previously have typically been prepared at a laboratory scale, often via solvent-processing or in situ polymerization techniques since they are amenable to small sample sizes.<sup>15,20,30,54-58</sup> One question for polymer scientists is whether the same materials can be produced on a much larger scale using conventional polymer processing techniques such as single-screw or twin-screw extrusion, compression or injection molding, or melt spinning. The present study arose

out of our attempts to make polymer-MWNT/CNF nanocomposites via twin-screw extrusion. To our surprise, the conductivities of extruded samples were disappointingly low. Indeed, an examination of the literature on this topic shows that a rather wide range of conductivity values have been reported,<sup>20,45,51,52,59</sup> and sometimes much lower than might be expected for a given particle loading. These differences can be attributed generally to the range of processing methods and conditions used by different authors. It is clear that processing affects the conductivity and also other material properties. The question then is: how can we maximize the conductivity of these materials and how can we recover the properties that might be lost after a processing step?

In this study, we show that a simple way to recover the electrical conductivities of polymer-MWNT/CNF nanocomposites following processing is by annealing the materials at a temperature exceeding the glass transition temperature ( $T_g$ ) of the polymer. The annealing step is shown to increase the room temperature conductivity by several orders of magnitude in some cases. Systematic effects on conductivity are observed as a function of annealing temperature and annealing time. Although similar observations have been mentioned in a couple of earlier studies,<sup>60,61</sup> this is the first detailed study on annealing effects to our knowledge. Our studies also explain why the conductivity is lost during processing in the first place, and why annealing increases it back. Specifically, the shear during processing tends to align the MWNT or CNF particles, which decreases their degree of interconnectivity and thereby the conductivity. When the material is annealed, however, the particle distribution becomes more isotropic and their connectivity thereby increases. The increase in connectivity due to annealing manifests

also as an improvement in the elastic character of the nanocomposites, which we detect through dynamic rheology experiments.

## 4.2. EXPERIMENTAL

**Materials.** Two polystyrene (PS)-based nanocomposites were investigated in this study. In one case, the polystyrene was Styron 666D from Dow Chemical, with a weight-average molecular weight of 240,000 g/mol and a polydispersity index of 2.29.<sup>62,63</sup> This was combined with multi-walled carbon nanotubes (MWNTs) purchased from Hyperion Catalysis International as a masterbatch with a mass concentration of 20% in PS. The second system consisted of high-impact polystyrene (i.e., a PS with 5 wt% copolymerized butadiene; weight-average molecular weight of 150,000 and polydispersity index of 2.73) obtained from Nova Chemicals and this was combined with carbon nanofibers (CNFs) (PR-19 from Pyrograf Products).

**Nanocomposite Sample Preparation.** For the PS/MWNT, appropriate amounts of the PS pellets and of the masterbatch pellets were mixed and fed into a twin-screw extruder (B & P Process Equipment; co-rotating, intermeshing, 25:1 L:D). The extruder was operated with a 400 rpm screw speed and a barrel temperature of 185°C in all zones except the last zone, which was held at 195 °C. Samples with MWNT mass concentrations of 1%, 2 %, and 4 % were prepared. For the PS/CNF, the PS pellets and the CNF were fed into a Werner-Pfleiderer twin-screw extruder (28 mm screw diameter, co-rotating, intermeshing, 30:1 L:D). Operating conditions were 60 rpm screw speed and 210°C barrel temperature all zones except the last zone (165°C). Samples with mass

concentrations of 3 %, 5 %, 7 %, 10 % and 15 % CNF were prepared. Samples for rheology and electrical conductivity measurements were prepared by compression molding the nanocomposite pellets in a Carver press. A circular die of diameter 25 mm and thickness 1 mm was used. The molding was done at a temperature of 150°C for 10 min at a pressure of about 0.9 MPa.

**Conductivity Measurements.** The electrical conductivity of the composites was measured in accordance with ASTM D4496. Samples of a known cross-sectional area and thickness were placed between copper electrodes and the DC resistance was measured using a Fluke 87 multimeter. The surfaces of the sample in contact with the electrodes were coated with silver paint in order to reduce discrepancies arising from micro-roughness. It was ensured that the surface area of the electrodes exceeded the cross-sectional area of the discs.

**Rheological Measurements.** Dynamic rheological experiments were performed on a RDAIII strain controlled rheometer (TA Instruments) equipped with a convection oven. A parallel plate geometry (25 mm diameter) was used with a gap of 0.9 mm. Frequency sweeps were obtained at 200°C for the PS/MWNT samples and at 170°C for the PS/CNF samples; the choice of temperature being dictated by the thermal degradation temperature of the matrix polymer. Frequency spectra from 0.032 rad/s to 320 rad/s were obtained at a strain of 0.5%, which was verified to be in the linear viscoelastic regime of the sample. Before recording each frequency sweep, the sample was equilibrated at the test

temperature usually for a period of 30 min. All rheological experiments were performed in a nitrogen atmosphere to avoid oxidative degradation of polystyrene.

**Confocal Microscopy Imaging.** Particle morphologies in the composite samples were evaluated using a laser confocal microscope (Carl Zeiss Model LSM510). The confocal microscope utilizes coherent laser light and collects reflected light exclusively from a single plane with a thickness of 100 nm (a pinhole sits conjugated to the focal plane and rejects light out of the focal plane). A red laser ( $\lambda = 633$  nm) was used as the coherent light and images were taken with an Epiplan-Neofluar 100x/1.30 oil-pool objective. A filter (Rapp Optoelectronic LP385) was used to limit the lower spectra of reflected light. One hundred two-dimensional images (optical slices with 512 pixels x 512 pixels), with scan size 92.1 x 92.1  $\mu\text{m}$ , were taken at a spacing of 100 nm by moving the focal plane. Images were further analyzed using the NIH Image software program.

## 4.3. RESULTS

### 4.3.1. Electrical Conductivity

Figure 4.1 presents the electrical conductivity  $\sigma$  at room temperature of PS/MWNT and PS/CNF nanocomposites before and after annealing. Consider the MWNT results first (Figure 4.1a). Recall that the samples were processed by twin-screw extrusion, followed by compression molding in a Carver press. For the unannealed samples, the conductivities were too low to be detected over the entire range of MWNT concentrations (the lower detection limit of our measurements is  $10^{-8}$  S/m). We will show later that these surprisingly low values of  $\sigma$  are due to the disruption of connectivity

between the particles. The significant result from Figure 4.1a is that the conductivity can be recovered by annealing at high temperatures. The choice of annealing temperature is crucial: we present  $\sigma$  for samples annealed at 170, 200, and 230°C for 30 min (note that these temperatures are higher than the  $T_g$  of PS ( $\sim 100^\circ\text{C}$ ), but well below its thermal degradation temperature ( $\sim 250^\circ\text{C}$ ). Annealing at 170°C is seen to have a modest effect:  $\sigma$  is increased for the 4% MWNT sample but not for the others. On the other hand, annealing at 230°C has a significant effect on  $\sigma$  at all MWNT concentrations. All the MWNT samples are now conductive, and the  $\sigma$  values approach ca. 1 S/m at the higher MWNT concentrations. Note that for the 4% MWNT sample, the conductivity is raised by several orders of magnitude to about  $10^{-2}$  S/m by annealing at 170°C, and by two more orders of magnitude to ca. 1 S/m by annealing at 230°C.

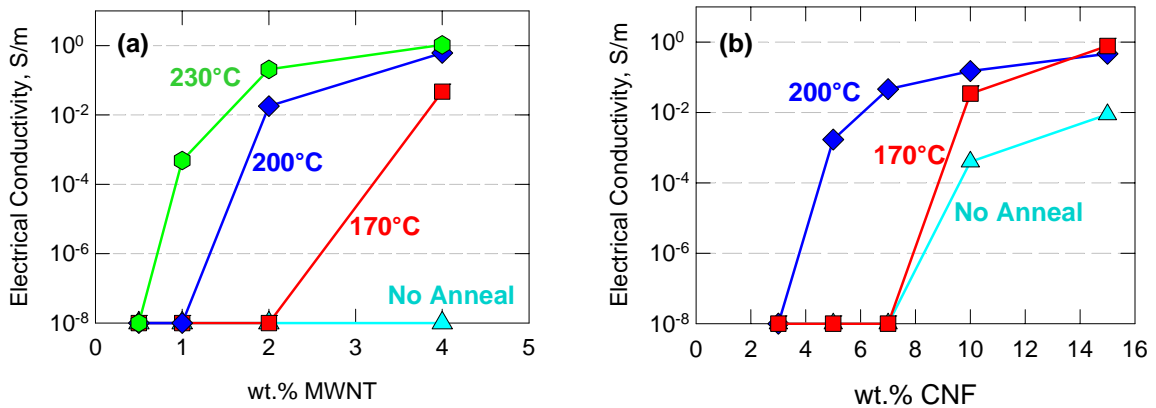


**Figure 4.1.** Effect of annealing temperature on electrical conductivity: (a) PS/MWNT and (b) PS/CNF. Samples were annealed for 30 minutes. Note the increase of many orders of magnitude in electrical conductivity.

Similar trends in electrical conductivity can be observed for PS/CNF samples (Figure 4.1b). Note that CNFs have a lower intrinsic conductivity as well as a lower

aspect ratio than MWNTs, and as a result, polymer/CNF composites have lower conductivities at a given particle loading compared to MWNT-based systems. Therefore, to obtain highly conductive polymer nanocomposites, one needs to use higher CNF loadings (note the higher values on the x-axis of Figure 4.1b). The effects of annealing are very similar, however. In the absence of annealing, we could only detect appreciable conductivities for the 10 and 15% CNF samples. For these two samples, annealing at 170°C for 30 min further enhances their conductivities by ca. two orders of magnitude. For the 5 and 7% CNF samples, annealing at 170°C has a negligible effect, but annealing at 200°C does impart significant conductivities.

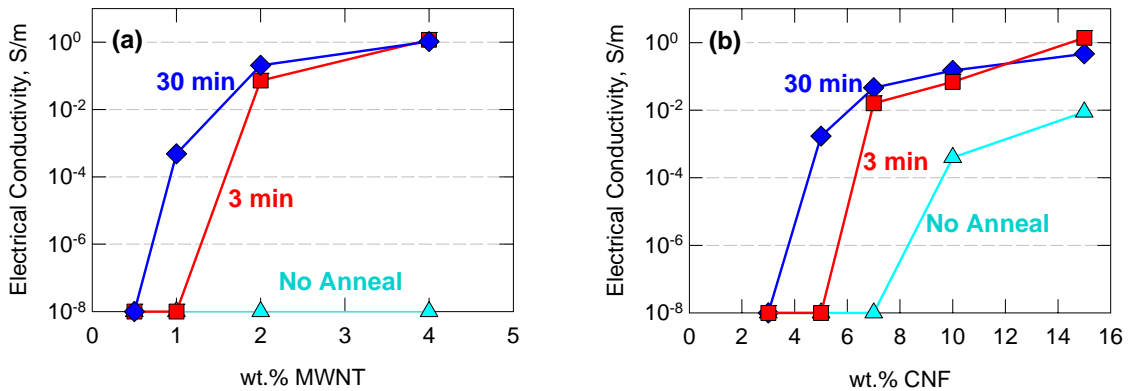


**Figure 4.2.** Effect of annealing time on electrical conductivity: (a) PS/MWNT annealed at 230 °C and (b) PS/CNF annealed at 200 °C. It takes longer to recover conductivity at low filler concentrations.

Figure 4.2 shows that in addition to annealing temperature, the annealing time also has an effect on the electrical conductivity of both PS/MWNT (Figure 4.2a) and PS/CNF (Figure 4.2b) composites. For the PS/MWNT samples, annealing time effects were investigated at 230°C. The data in Figure 2a show that the 4% PS/MWNT sample

attains the same conductivity whether it is annealed for 3 min or 30 min at this temperature. On the other hand, the 2% MWNT sample has a lower conductivity after a lower annealing time. The 1% sample remains an insulator if annealed for just 3 min, but becomes conductive after annealing for 30 minutes. Similarly, for the PS/CNF samples, annealing for a lower time of 3 min at 200°C is sufficient for the 15% CNF sample, but at the lower CNF concentrations a longer annealing time of 30 min is necessary to fully restore the conductivity.

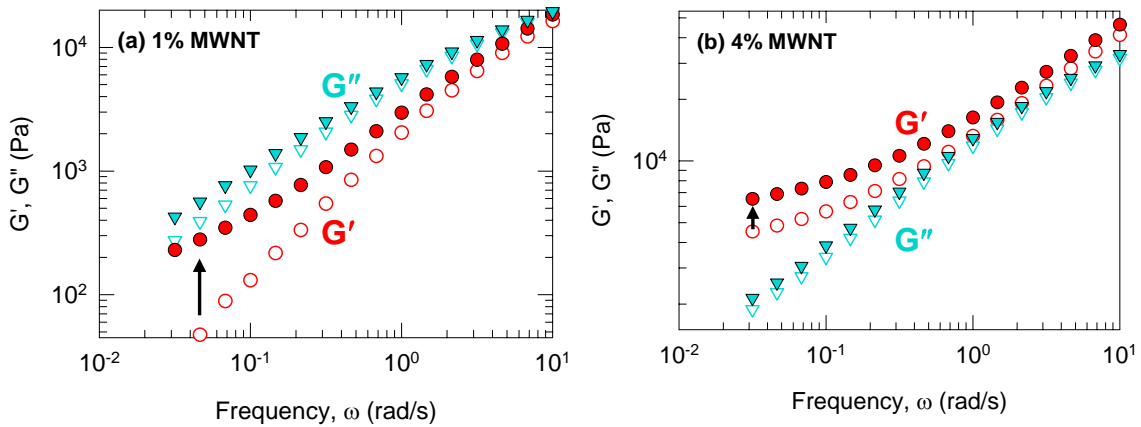


**Figure 4.3.** Effect of annealing on the dynamic rheological properties at 200°C of PS/CNT nanocomposites containing (a) 1 wt.% CNT and (b) 4 wt.% CNT. Data are shown for the elastic modulus  $G'$  (circles) and the viscous modulus  $G''$  (triangles) as functions of the frequency  $\omega$  for an unannealed sample (open symbols) and a sample annealed at 230°C for 30 min (filled symbols). In each case,  $G'$  at low  $\omega$  is increased by annealing, as shown by the arrows.

### 4.3.2. Dynamic Rheology

We will show that the above recovery of conductivity in MWNT and CNF-based nanocomposites after annealing is due to the re-establishment of connections between the particles that were lost during processing. One way to establish the above link between properties and microstructure, is to examine the dynamic rheology of samples before and

after annealing. Dynamic rheology (measurements of the elastic modulus  $G'$  and the viscous modulus  $G''$  as functions of the frequency  $\omega$ ) is a sensitive probe of the percolated network formed by particles in polymer nanocomposites. The presence of such a network manifests as a plateau in the elastic modulus  $G'$  at low  $\omega$ , and the magnitude of this  $G'$  plateau is known to correlate with the density of connections in the network.

Figure 4.3 shows frequency sweeps at 200°C for selected PS/MWNT samples prior to and after annealing at 230°C for 30 min. The results are especially notable for the 1% MWNT sample (Figure 4.3a). In this case, the unannealed sample does not show a low- $\omega$  plateau in its  $G'$ , which implies the absence of a MWNT network in this sample. This observation helps to explain why this unannealed sample showed negligible conductivity in Figure 4.1a. On the other hand, upon annealing, the  $G'$  plot levels off at low  $\omega$ , suggesting that a sample-spanning MWNT network has been established. Comparing the two sets of data, at the lowest  $\omega$ , the value of  $G'$  is increased by a factor of 5 due to annealing. Correspondingly, annealing also induces a small increase in the viscous modulus  $G''$ . Generally, network connectivity is primarily reflected in the elastic properties of the sample, which is why more significant changes are observed for  $G'$  than  $G''$ . Similar increases in  $G'$  at low  $\omega$  are also found at other MWNT concentrations and also for the CNF-based samples. For illustration, we also show data before and after annealing for the 4% MWNT sample in Figure 4.3b. In this case, there is already a  $G'$  plateau at low  $\omega$  for the unannealed sample, implying that a percolated MWNT network does exist. Upon annealing, the  $G'$  plateau increases in magnitude, indicating a higher density of network connections.

It should be noted that the rheological data in Figure 4.3 are taken at 200°C – so the samples do get annealed at this temperature during experimentation. Thus, it is not a straightforward matter to compare annealed and unannealed samples using melt rheology. Indeed, it is then understandable that the differences in rheology at 200°C are much more modest than the differences in room-temperature conductivities between the unannealed and annealed samples. Nevertheless, our rheological data are reproducible and consistent, i.e., the annealed sample is always the one that exhibits the higher moduli.

### **4.3.3. Confocal Microscopy**

The dynamic rheological data are consistent with the hypothesis that interparticle connections are restored during annealing. To further substantiate this, we have directly visualized the structure in our composites using confocal microscopy. The MWNTs used in our study were too small to be individually resolved by this technique (the pictures obtained were similar to those we have reported earlier<sup>64</sup>). However, the larger CNFs can be resolved quite nicely, and Figure 4.4 shows typical micrographs of both unannealed (Figure 4.4a) and annealed (Figure 4.4b) PS/CNF samples. The unannealed sample clearly shows substantial alignment of the CNFs. This is further illustrated in the Fourier transform of the image, which shows an anisotropic pattern that is elongated normal to the alignment direction. Thus, it is clear that the CNF particles are significantly aligned, presumably due to the shear involved in the processing steps (i.e., extrusion, followed by compression molding). In contrast, the annealed sample (Figure 4.4b) shows an isotropic distribution of the CNFs and the Fourier transform of this image shows an isotropic pattern. Thus, the confocal images show that the action of annealing is to restore an

isotropic distribution of particles, which, in turn, implies the re-establishment of connections in the particle network.

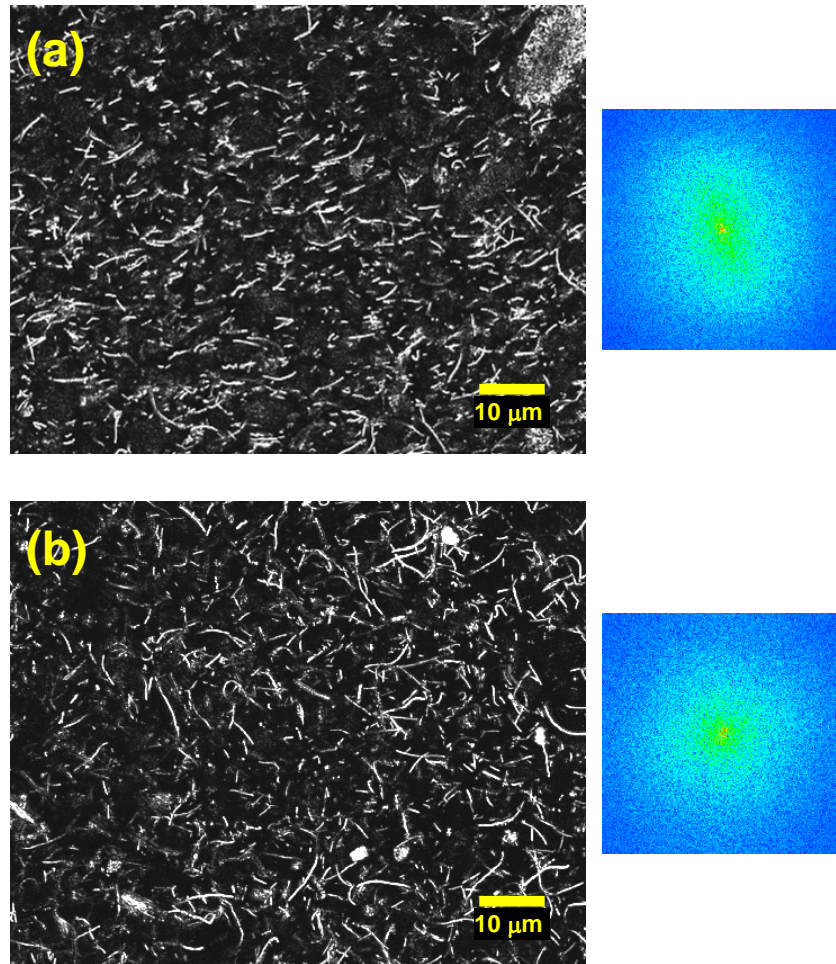


**Figure 4.4.** Confocal microscopy images showing the effect of annealing on the microstructure of PS/CNF nanocomposites containing 3 wt.% CNF. (a) Unannealed sample, showing alignment of CNFs, as confirmed by the elongated Fourier transform of this image, shown on the right. (b) Annealed sample, showing a more isotropic orientation of the CNFs, as also seen from the isotropic shape of the Fourier transform image on the right.

#### 4.4. DISCUSSION

We have demonstrated the strong influence of conventional polymer processing techniques on the properties of polymer-MWNT and polymer-CNF nanocomposites.

Both the conductivity and rheological properties are adversely affected by processing. However, these properties can be restored to their expected levels by a high-temperature annealing treatment. To our knowledge, this is the first detailed investigation of annealing effects on MWNT/CNF-based composites, especially in showing how changes in material properties are directly connected to changes in the microstructure. Our key finding is that connections in the particle network are lost during processing because the particles become aligned in the flow direction. The idea that alignment implies a loss of particle interconnects, thereby delaying the onset of particle percolation in the matrix, has been advanced by others.<sup>65</sup> Similarly, other researchers have separately shown that particle alignment induced by high shear can adversely impact the dynamic rheological properties<sup>57</sup> and even the conductivity of polymer/MWNT composites.<sup>45,55,56,66</sup> These studies, however, did not deal with the effects of annealing to restore the lost properties. To our knowledge, the impact of annealing on conductivity in polymer/MWNT materials has only been considered in passing in a couple of papers,<sup>60,61</sup> but has not been the focus of any study thus far.

Finally, it is worth considering how or why annealing is able to re-orient the aligned particles into an isotropic state. Nanocomposites are typically non-Brownian systems due to their high matrix viscosity and the extended geometry of the filler particles.<sup>45,65,67,68</sup> Nevertheless, while translational diffusion may be limited, the particles may still be able to rotate and re-orient, even under non-Brownian conditions. Annealing at higher temperatures will promote such re-orientation because of the decrease in matrix viscosity and the increased thermal diffusivity. Moreover, the relaxation of polymer

chains at these high temperatures will also facilitate the re-arrangement of the dispersed nanoparticles. Note from our data (Figures 4.1, 4.2) that the nanocomposites with higher particle concentrations recover their conductivity after annealing at lower temperatures and for shorter times. At higher concentrations, the particles are sufficiently close to each other that they can re-form interconnects quite easily. However, at lower concentrations, the particles need to re-orient and/or diffuse appreciable distances to form a link with their nearest neighbors. Similar reorganization under quiescent conditions at high temperatures (after shear, for example) has been reported for clay particles in polymer/clay nanocomposites.<sup>67,68</sup> A further driving force for the re-orientation of clay particles was postulated to arise from strong attractive interaction between particles.<sup>68</sup> This may be a factor in the present study as well, since it is known that MWNTs and CNFs experience stronger van der Waals interactions than clay particles due to their highly conductive nature.

## 4.5. CONCLUSIONS

In this study, we have shown that the conductivity of PS/MWNT and PS/CNF nanocomposites is decreased as a result of processing (by twin-screw extrusion and compression molding), but can be recovered by annealing at high temperatures. Similarly, the dynamic rheological properties, specifically the elastic modulus  $G'$  at low frequencies, can also be increased by annealing. The microstructural basis for the above results is that, during processing, the particles become aligned in the flow direction, leading to a decrease in the connectivity of the particle network. The same connections, however, are re-established during annealing, which explains the recovery of the

properties. Direct evidence for the above mechanism has been obtained by confocal microscopy. We believe that our results may have practical relevance for the large-scale manufacture of conductive polymer nanocomposites.

# Chapter 5

## EFFECT OF CLAY FRACTIONATION ON NANOCOMPOSITE PROPERTIES

### 5.1. INTRODUCTION

In this Chapter, we focus on polymer nanocomposites consisting of organoclay platelets dispersed in a polymer matrix. As discussed in Chapter 2, clay particles can be true nanoscale fillers if they are dispersed at a single platelet level, which is referred to as the exfoliated morphology (see Figure 2.4).<sup>9,69</sup> If the quality of dispersion is not as good, the morphology may be of the intercalated or phase-separated type. The exfoliated morphology is clearly the preferred one since it is only in this case that the clay particles have a large aspect ratio.<sup>33</sup> Indeed, as shown by Chapter 3, large-aspect-ratio particles are the ones that provide the matrix with the greatest property enhancement.<sup>32-37,70</sup> In practice, this ideal exfoliated morphology is never completely achieved and instead the composite contains both individually dispersed clay platelets and stacks of such platelets. Stacks of clay platelets (also called “tactoids”) have a lower aspect ratio due to the stack thickness, and are less effective towards enhancing polymer properties.

Current efforts to maximize dispersion, and hence effective aspect ratio, of clay platelets in polymers have focused on the type of surface modification conferred to the clay.<sup>9</sup> It is known that the clay surface must be rendered hydrophobic by surfactant modification in order to ensure good dispersion in polymers. Thus, emphasis has been

placed on the type of surfactant (one or two-tail, ammonium or imidazolium headgroup etc.) and the chain length of the surfactant as variables that can impact the dispersion of clays.<sup>71</sup> Others have found that exfoliation can be achieved by covalently tethering the matrix chains onto the clay surface.<sup>72</sup> Currently, surfactant-modified montmorillonite clays (“organoclays”) are commercially available from companies such as Southern Clay Products and Nanocor Inc. For each variety of organoclay, the manufacturer specifies that the material has been obtained by treating the native montmorillonite (MMT) with a given surfactant, such as ditallow dimethyl ammonium chloride (DDAC). These organoclays have been quite popular due to their low cost and the wide variety of property enhancements they can confer. However, one still needs to use appreciable amounts of organoclays (ca. 5-10%) to sufficiently enhance properties, and moreover, organoclays greatly impair the clarity (transparency) of the resulting polymer material. The lack of transparency suggests that all the clay is not being dispersed at the nanoscale. The question then is: can we improve the dispersion of clay particles in polymers and thereby improve their efficiency?

In this study, we demonstrate a simple method to substantially improve the properties of polymer-organoclay composites. This method involves fractionating the clay to remove large aggregates. Our method is predicated on the fact that the native MMT (and hence also, all organoclays) are highly polydisperse mixtures of various particle sizes. Commercial organoclays are made by dispersing (exfoliating) the MMTs in water and then adding a surfactant to modify the clay surface. However, we observed that aqueous dispersions of MMT in water are highly turbid and large particles/aggregates are

visible in these samples by optical microscopy. In other words, there are large structures that simply cannot be exfoliated further at the nanoscale in aqueous MMT dispersions. We therefore use a conventional centrifuge to remove these large aggregates from the MMT dispersion. The remaining particles constitute the smaller and/or less aggregated fraction of the clay, which we call fractionated montmorillonite or FMT. We then treat this FMT with DDAC surfactant to obtain its organoclay counterpart (o-FMT). The o-FMT is then combined with polystyrene (PS), and the resulting composites are characterized using diffraction and microscopy techniques. We then evaluate their properties such as transparency, rheology and flammability behavior and draw comparisons with composites prepared with commercially available organoclay (also modified by DDAC).

## 5.2. EXPERIMENTAL

**Fractionation of MMT.** The MMT used was Sodium Cloisite from Southern Clay Products. Dispersions of this MMT (4 wt.%) were prepared in distilled-deionized water by stirring continuously using a magnetic stirrer for three days. This dispersion, which was a milky viscous liquid (see Figure 5.1) was centrifuged for 1 h at 3200 g. The precipitate from this centrifugation step contains the largest clay particles and aggregates (~ 20% of the starting material) and we will refer to it as large montmorillonite (LMT). The supernatant from this centrifugation was a translucent fluid, and was then further centrifuged for an additional hour at 18,500 g. The precipitate from this second centrifugation step was collected, while the supernatant was discarded. The clay in the

precipitate is what we will refer to as fractionated montmorillonite (FMT). For a given amount of starting material, about 50% was FMT.

**Particle Characterization.** The average sizes of the clay particle fractions (FMT and LMT) were measured using dynamic light scattering (DLS) on a Photocor-FC instrument. Dispersions of FMT and LMT in water were also characterized by optical microscopy using a Zeiss Axiovert 100 TV inverted microscope with a 20X objective and by TEM using a JEOL JEM-2100F microscope. For TEM, a very dilute dispersion of each clay (0.05 wt%) was made and a drop of this dispersion was dried on a copper grid.

**Synthesis of Organo-FMT (o-FMT).** The FMT from above was diluted to 1.5 wt.% with distilled-deionized water and heated to 65°C. Simultaneously, DDAC (trade name Arquad, from Fluka) was dissolved in a 450 mL mixture of 60:40 water/ethanol by heating to 65°C. The amount of DDAC added to the FMT dispersion corresponded to twice the cation exchange capacity of the native MMT, known to be 92.6 milliequivalents per 100 g of clay. The clay was allowed to react with the DDAC overnight with constant stirring. The o-FMT was then precipitated, recovered by vacuum filtration and dried. Excess DDAC from the o-FMT was removed by Soxhlet extraction in ethanol for three days. The o-FMT was then dried prior to use.

**Purification of Commercial Organoclay.** We compared the o-FMT to a the commercial organoclay, Cloisite 15A, also from Southern Clay Products. The Cloisite 15A product is obtained by treating the native MMT with DDAC, and is known to contain up to 36 %

excess of DDAC relative to its cation exchange capacity. The excess DDAC was removed by Soxhlet extraction in ethanol much like with the o-FMT. The purified Cloisite 15A was then dried prior to further use.

**Preparation of Nanocomposites.** Polymer-clay nanocomposites were prepared by combining o-FMT or the purified Cloisite 15A with a high molecular weight PS (Styron 666D, Dow Chemical). The PS had a mass-average molecular weight of 240,000 g/mol with a polydispersity index of 2.29.<sup>62,63</sup> PS/clay nanocomposites were prepared by a solvent casting method. A dispersion of 1% organoclay in chloroform was prepared by sonication for 5 min, followed by stirring for 2 h. A solution of 10 wt% PS in chloroform and the organoclay dispersion were combined, and the mixture was stirred for 24 h. Thereafter, the mixture was cast into an aluminum foil pan and the chloroform evaporated in a hood overnight. The nanocomposite was then further dried and annealed at 160°C in a vacuum oven for 48 h.

**XRD.** X-ray diffraction spectra on polymer-clay nanocomposites were collected on a Phillips diffractometer using Cu-K $\alpha$  radiation ( $\lambda = 1.54 \text{ \AA}$ ) with a  $2\theta$  step of 0.04° and a 3 s count time per step. Samples for XRD were prepared by hot pressing nanocomposites into 2 mm thick plates. The stacking distance  $d$  of the clay in the nanocomposites was determined from the position of the peak at lowest  $2\theta$  using Bragg's law,  $d = \lambda / 2 \sin\theta$ .

**TEM.** The microstructures of the polymer clay nanocomposites were observed by using a JEOL JEM-2100F TEM coupled with a Gatan CCD camera operating at 200 kV.

Specimens of 60 nm thickness were prepared by ultramicrotoming (Leica UC-6) with a Diatome diamond knife (Hatfield, PA).

**Transparency Measurements.** The transmittance of composite films was characterized by a Varian Cary 50 UV-Vis spectrophotometer (Palo Alto, CA) with scanning wavelength ranging from 200 to 800 nm. The film thickness was 200  $\mu\text{m}$ .

**Rheology.** PS/clay samples were prepared by hot pressing into discs of 25 mm diameter and 1 mm thickness at a temperature of 140°C and a pressure of 4 metric tons. Rheological experiments were performed on an RDA-III strain-controlled rheometer (TA Instruments) equipped with a convection oven at 180°C. All experiments were conducted in a nitrogen atmosphere to limit oxidative degradation of the polymer. A parallel plate geometry (25 mm diameter) was used at a gap of 0.9 mm. Measurements were performed under dynamic oscillatory shear. Dynamic frequency sweeps were conducted within the linear viscoelastic regime of the sample, which was determined separately from strain sweep experiments.

**Flammability.** Cone calorimetry and radiant gasification experiments were conducted on the polymer-clay nanocomposites. The experimental procedure was identical to that described in Chapter 3.

## 5.3. RESULTS AND DISCUSSION

### 5.3.1. Clay Fractions in Water

Clays are known for their ability to gel water.<sup>7,73</sup> However, their efficiency at gelation varies with clay type. For instance, laponite (a synthetic clay consisting of 30 nm disks) is known to form clear gels in water at concentrations as low as 1.5 wt%. The high efficiency of laponite is attributed to its high chemical purity, low polydispersity, and highly hydrophilic surface – indeed, laponite is known to get exfoliated in water into individual discs.<sup>74,75</sup> In contrast, MMT is highly polydisperse and has some chemical impurities.<sup>73</sup> Based on the turbidity of aqueous MMT dispersions, there is likely to be incomplete exfoliation of the MMT layers. It is reasonable, therefore, to expect MMT to be less efficient at gelling water than laponite.

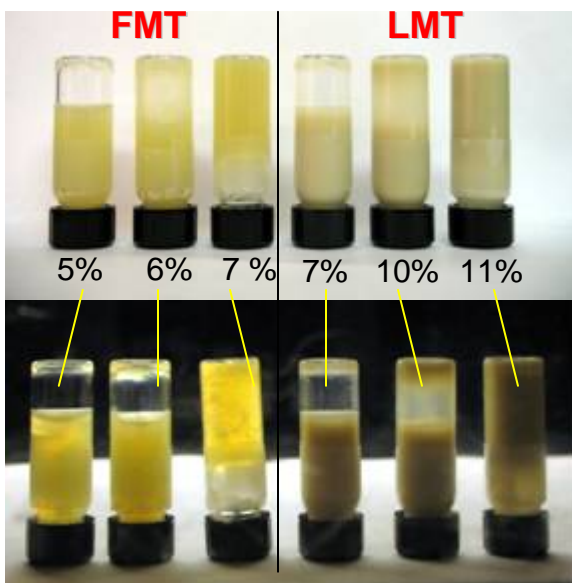


**Figure 5.1.** Comparison of aqueous dispersions of FMT and LMT. LMT forms gels around 11%, whereas FMT gives rise to gels at 7%, based on the tube inversion test (top). Under crossed polarizers, the 7% FMT gel displays birefringence.

Our studies show that there are significant differences between the MMT fractions in their ability to gel water. Figure 5.1 shows photographs of aqueous dispersions containing either the large MMT particles (LMT) or the small MMT particles obtained after fractionation (FMT). Note that the LMT dispersions are opaque and display a brown hue whereas the FMT dispersions are translucent and display a yellowish color. Additionally, on vial inversion, samples with 7% or more of FMT do not flow, whereas the threshold is 11% for LMT. Vial inversion is often used as a simple measure of gelling ability<sup>76</sup> – therefore, the data suggest that FMT is much more efficient at gelation than LMT. Also displayed in Figure 5.1 are images of the same samples under crossed polarizers (bottom). What is interesting is that the 7% FMT gel shows birefringence, presumably due to alignment of particles. No such birefringence can be observed for LMT gels. In this context, it is worth pointing out that birefringence is observed in concentrated aqueous dispersions of laponite and this has been attributed to an isotropic to nematic transition of the system.<sup>77</sup>

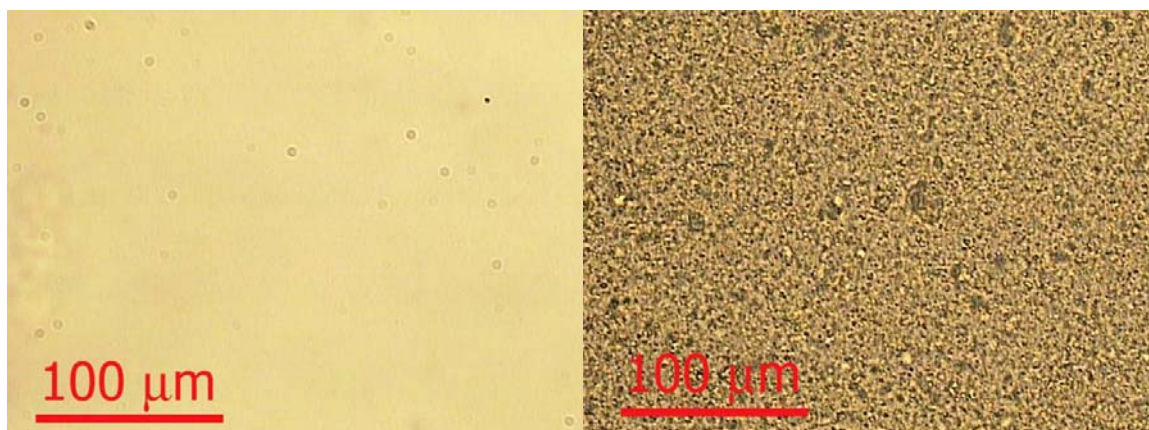


**Figure 5.2.** Optical microscopy images of aqueous dispersions of FMT (left) and LMT (right). Despite being larger in size, the effective aspect ratio in LMT dispersions is lowered by the formation of aggregates which can be seen in the image. Left: FMT. Right: LMT.

We also determined an average particle size in both the FMT and LMT samples using DLS. These studies were done on aqueous dispersions with particle concentrations of 0.5% and 1%. The average hydrodynamic radius was found to be 540 nm for the LMTs and 380 nm for the FMTs. Further characterization was done using optical microscopy and TEM. In Figure 5.2 we show bright-field microscopy images of FMT and LMT gels. The FMT gel appears free from aggregates whereas the LMT gel displays numerous aggregates that are about 1 – 5  $\mu\text{m}$  in size. Note that the image of the LMT gel is darker because the sample is turbid and therefore the transmission of light is quite low. Finally, Figure 5.3 shows a TEM image of FMT platelets on the left, and we observe a number of platelets, roughly 300 nm in size. On the right is a TEM image of the LMT, showing a large aggregate. Many such aggregates were seen in the LMT whereas these were mostly absent in the FMT. Taken together, our studies show that the LMT fraction contains the largest clay particles as well as many large aggregates, while the FMT fraction is largely composed of individual clay platelets.

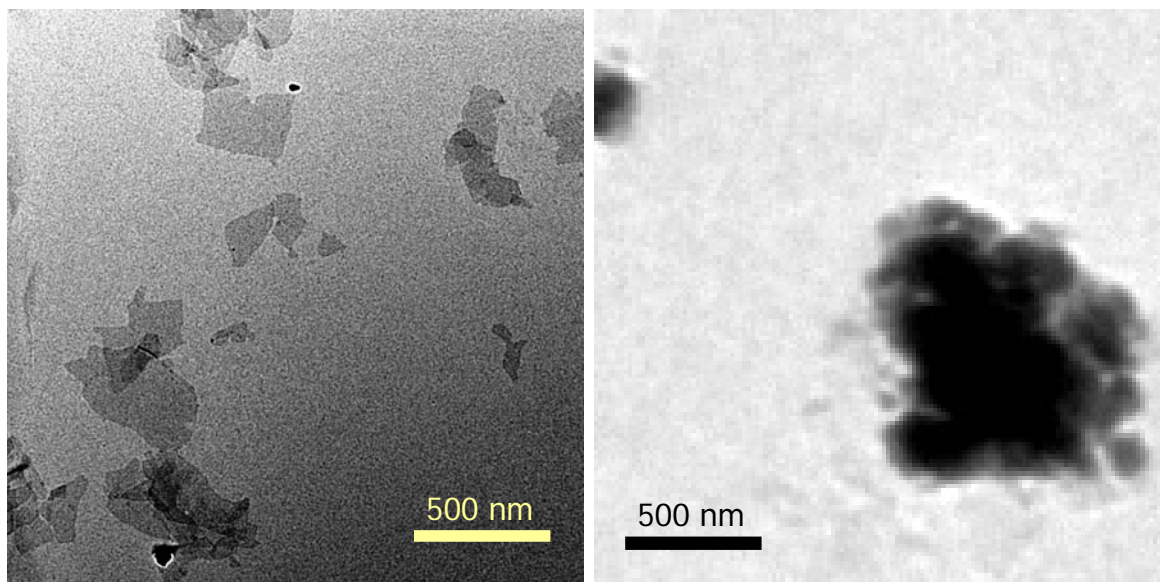


**Figure 5.3.** TEM images of FMT (left) and LMT (right). The particles were dried on the grid from their dilute aqueous dispersions.

### 5.3.2. Nanocomposite Morphology

We now describe studies with PS nanocomposites made using o-FMT and Cloisite 15A (henceforth referred to simply as “15A”). First, we characterize the morphology of the nanocomposites using XRD (Figure 5.4) (clay concentration of 5%). Both the PS/15A and PS/o-FMT samples show Bragg reflections in their XRD spectra. For the PS/15A, the gallery spacing is 30 Å, while for the PS/o-FMT it is 31.5 Å. Both these values are larger than the gallery spacing of 23.5 Å for the 15A clay powder. The increase in gallery spacing indicates that the polymer chains have intercalated between the stacks in the clay platelets.<sup>9</sup> Thus, both nanocomposites have an intercalated morphology and the intergallery spacing agrees with that found in previous studies of PS/organoclay composites.<sup>69,78</sup>

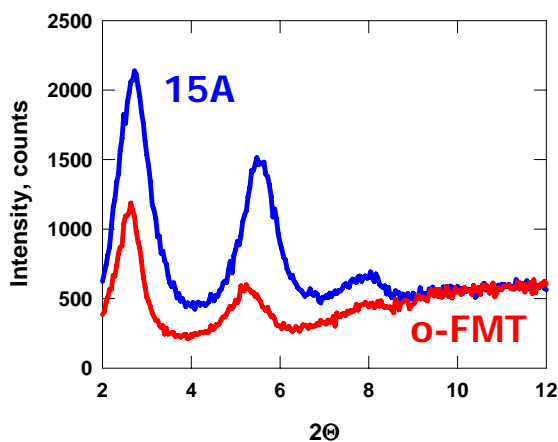


**Figure 5.4.** XRD spectra for nanocomposites containing 5 weight % organoclay. Both nanocomposites have an intercalated morphology and the effect of clay size on polymer intercalation is negligible.

Next, we turn to TEM to visualize the nanocomposite morphology directly. Representative images of PS/o-FMT and PS/15A samples, each at 5% organoclay, are

shown in Figure 5.5. Figure 5.5a reveals the homogeneous distribution of clay tactoids in the PS/o-FMT composite. On the other hand, Figure 5.5c reveals that the PS/15A composite contains aggregates that are nearly 1  $\mu\text{m}$  in size. A close up of a PS/o-FMT clay tactoid in Figure 5.5b reveals that it contains a few number of clay layers, whereas a close up of a PS/15A aggregate in Figure 5.5d reveals a large number of clay platelets. Thus, the TEM images clearly show the better dispersion of organoclay in the PS/o-FMT composites than in the PS/15A composites.

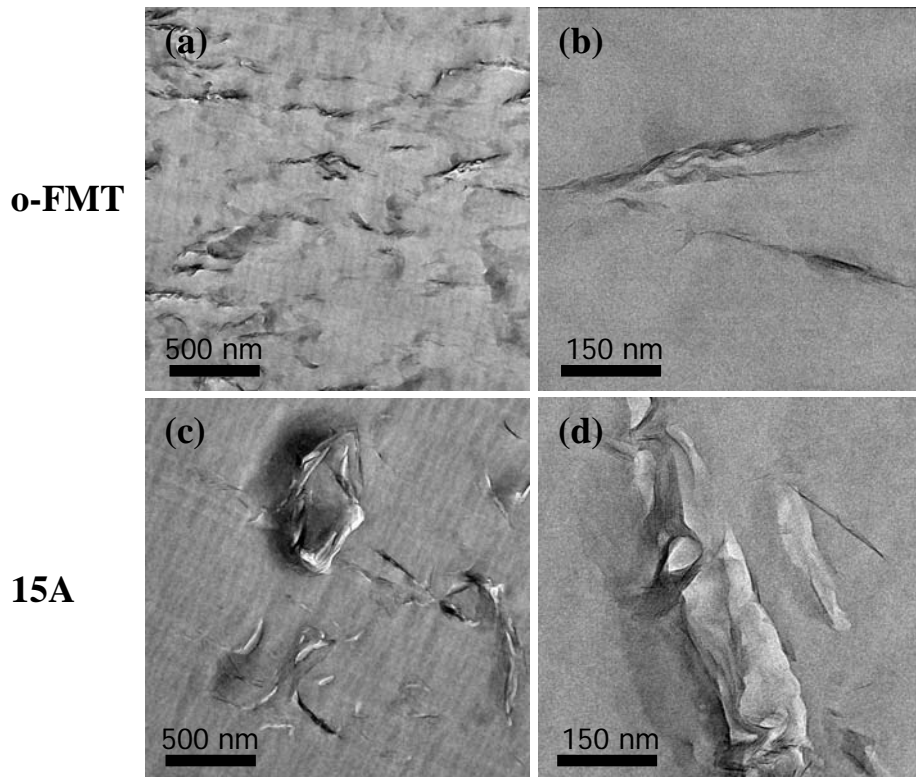


**Figure 5.5.** TEM images for nanocomposites containing 5% organoclay: (a) and (b) PS/o-FMT; (c) and (d) PS/15A.

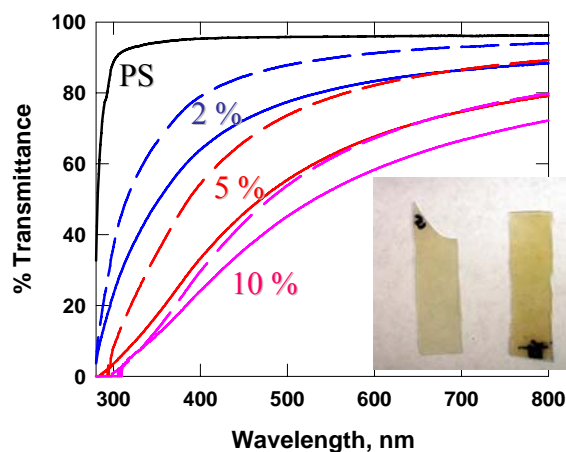


**Figure 5.6.** Transmission of visible light through 200 nm thick nanocomposite films of PS/o-FMT (dashed line) and PS/15A (solid line). The transmission is higher across the wavelength range for samples containing o-FMT than for those containing 15A.

### 5.3.3. Nanocomposite Transparency

Next we evaluate the difference in transparency between the PS/o-FMT and PS/15A composites. The % transmission is shown as a function of wavelength for the two types of composites at various particle loadings in Figure 5.6. At all wavelengths, the PS/o-FMT composites display higher transmission values. The difference in transmission between the two types of composites is significant: the 5% PS/o-FMT has roughly the same transmission as the 2% PS/15A, and the 10% PS/o-FMT has roughly the same transmission as the 5% PS/15A. The inset shows a photograph comparing the two types of composites, and it is evident that the PS/o-FMT sample is more transparent. The increased transparency of PS/o-FMT composites is apparently the result of excluding the largest MMT aggregates.

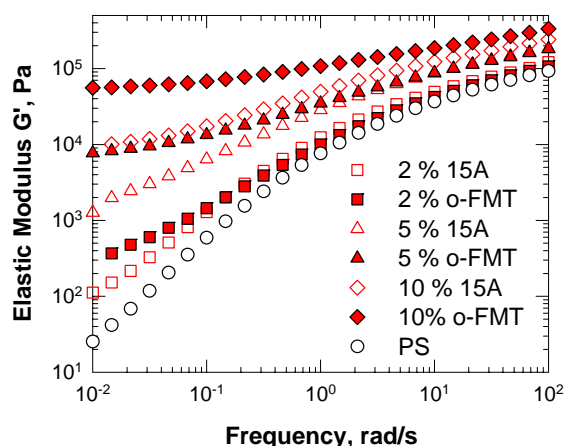


**Figure 5.7.** Dynamic rheology at 180°C of PS nanocomposites containing o-FMT and 15A. The elastic modulus  $G'$  is much higher for the o-FMT samples at the same loading.

### 5.3.4. Viscoelastic Properties

The differences between o-FMT and 15A are most dramatically seen in the melt rheology of the nanocomposites. Figure 5.6 shows the elastic modulus  $G'$  as a function of frequency  $\omega$  for the parent PS polymer and for the PS/15A and PS/o-FMT composites at various clay loadings. Note that  $G'$  is shown because it is the parameter that most reflects the rheological changes upon clay addition. The parent polymer exhibits a viscous response with the  $G'$  scaling at low  $\omega$  in a manner characteristic of viscous fluids, i.e., with  $G' \sim \omega^2$ . Adding clay particles causes a systematic increase in  $G'$ , especially at low frequencies, where  $G'$  becomes less frequency-dependent. At the higher clay loadings,  $G'$  approaches a low- $\omega$  plateau, which means that the sample relaxes very slowly at long time scales.<sup>9,68,72,78,79</sup> Such behavior is characteristic of a volume-filling “jammed” network of particles in the nanocomposite.<sup>65</sup>

The significant result from Figure 5.7 is that  $G'$  for the PS/o-FMT composites are higher than for those containing 15A at all clay loadings. At a 5% loading, the  $G'$  for PS/o-FMT is larger than that of PS/15A by a factor of 3 while at a 10% loading, the difference is a factor of 5. In effect, 5% of o-FMT gives a rheology similar to that obtained by adding 10% 15A. These results starkly illustrate the superior efficiency of the o-FMT. The differences can also be seen in a plot of the complex viscosity  $\eta^*$  as a function of frequency  $\omega$  in Figure 5.8. As clay is added,  $\eta^*$  increases at low  $\omega$ , mirroring the increase in  $G'$ . Again, the  $\eta^*$  is much higher for the PS/o-FMT composites, with the increase being by a factor of 5 at low  $\omega$  for the 10% sample. The rheology data thus indicate that o-FMT is more effective than 15A in the formation of jammed networks. Presumably, this difference is because more of the o-FMT particles are participating as crosslinks in the network, whereas much of the 15A exists in the form of large aggregates and is thereby ineffective at network formation.

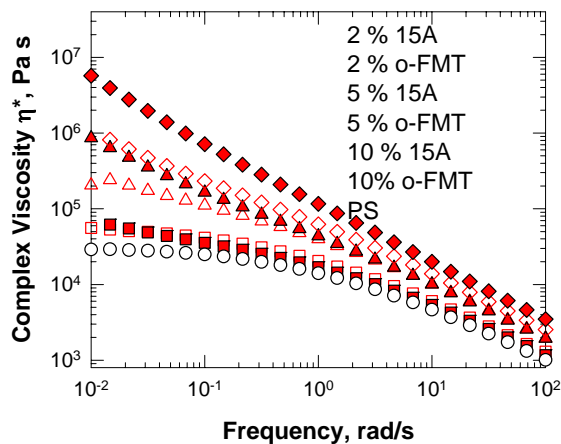


**Figure 5.8.** Complex viscosity data for nanocomposites containing o-FMT and 15A. The o-FMT nanocomposites display higher values of complex viscosity than those prepared with 15A at the same loading.

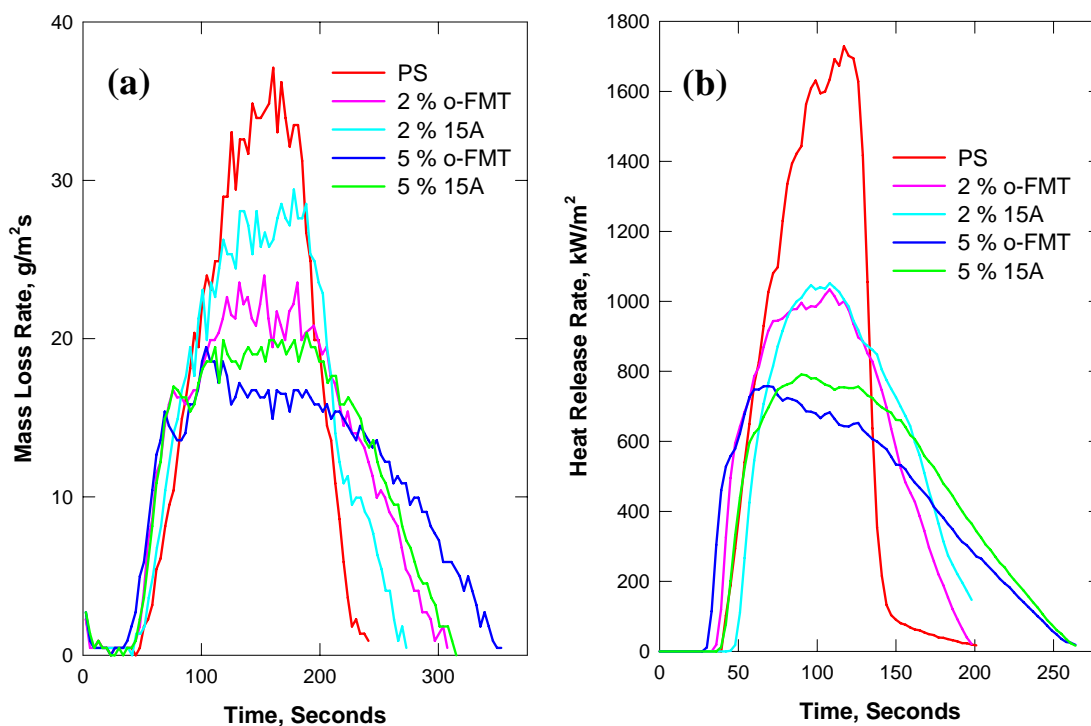


**Figure 5.9.** (a) Mass loss rate of PS/o-FMT and PS/15A. The nanocomposites containing o-FMT display lower values of mass loss rate, about 20%. (b) Heat release rate profiles for both types of composites.

### 5.3.5. Flammability Behavior

The mass of a sample was continuously measured when exposed to an external radiant flux of  $50 \text{ kW/m}^2$  in a slow flowing nitrogen atmosphere and the mass loss rate was calculated by taking the time derivative of the measured weight change. The results with PS/o-FMT and with PS/15A at 2 % and 5 % mass concentrations of the organoclay are shown in Figure 5.9a. During the gasification experiment, PS behaved like a liquid. Numerous bubbles were seen and after the test no char was left in the container. Similarly, samples with 2 wt. % organoclay concentration behaved like a viscous liquid with accompanying formation and bursting of many large bubbles except that many solid

grey islands were formed. Such islands remained at the end of the test and their pictures are shown in Figure 5.10. The size of the islands was larger in the case of PS/o-FMT. Correspondingly, the 2 wt. % PS/o-FMT exhibited a lower mass loss rate than the PS/15A. At 5 wt. % loading, the PS/o-FMT behaved almost like a solid with a wavy surface contour and with few deep cracks. In contrast, the 5 % PS/15A formed numerous islands and the aluminum pan can be seen clearly between the islands. Accordingly, the 5 % PS/o-FMT showed a lower mass loss rate than the 5 % PS/15A although the improvement was modest as shown in Figure 5.9a.

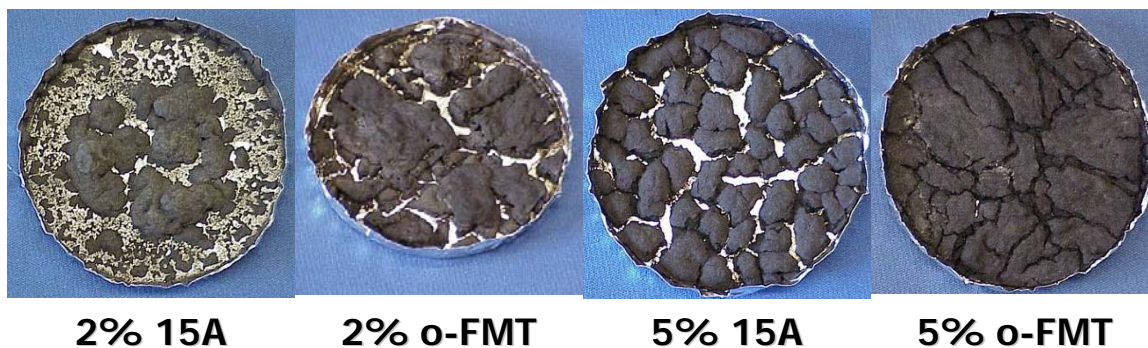


**Figure 5.10.** Residues of PS/15A and PS/o-FMT after a gasification experiment. Residues of samples containing o-FMT exhibit larger islands or lesser cracks; conversely, less of the aluminum pan is visible in the FMT residue images.

It has been demonstrated that the flame retardant performance of polymer nanocomposites is mainly due to the physical process of heat shielding by the formation of a network-structured protective layer in the condensed phase.<sup>3,23,27</sup> Therefore, the same trends in mass loss rate with clay type and loading are expected in the heat release rate curves shown in Figure 5.9b. For a fixed mass concentration, the heat release rate curves are almost identical for the two types of organoclay. After the gasification experiments,

the PS/o-FMT composites definitely formed residues that had less cracks and were larger in size as seen in Figure 5.10. The 5 % PS/o-FMT sample exemplifies the relationship between network formation in the initial sample as measured by  $G'$  (Figure 5.7) and the formation of a solid protective layer which was nearly uniform. In contrast, the 5 % PS/15A had lower  $G'$  and in turn produced less of a protective layer. At present, it is not clear why the improved residue formation did not translate into much lower mass loss and heat release rates of the PS/o-FMT composites. However, we point out that in a study of the effect of aspect ratio on the flammability of clay nanocomposites, large differences in flammability metrics were observed between MMT and synthetic mica ( $\sim 10$  fold increase in aspect ratio compared to MMT<sup>48</sup>) consistent with previous observations that the aspect ratio of the filler dictates flammability behavior to a large extent.<sup>3,37,64</sup> In light of these findings, we speculate that the effective aspect ratio does not vary significantly between the PS/o-FMT and PS/15A even when more of the o-FMT particles are participating in the network.

## 5.4. CONCLUSIONS

In this study, we have presented a simple method to substantially improve the efficiency of clay particles as a nanoscale filler for polymers. We have shown that, by excluding the large particles and aggregates from a commercial clay, we can obtain a fractionated montmorillonite (FMT) that, when organically modified, disperses better into polystyrene. The resulting PS/o-FMT nanocomposites are more transparent and display significantly higher elastic moduli compared to PS nanocomposites prepared with an equivalent commercial organoclay. The flammability properties of the PS/o-FMT also

appear to be slightly improved – in particular, greater amounts of residue are left behind when the materials are burned. The improvement in properties with the o-FMT is presumably because the particles are more effective at building a particle network, i.e., in terms of increasing the connectivity of the network. We suggest that the effectiveness of o-FMT particles should also extend to their dispersions in non-polar solvents, such as for the creation of greases and paints at a low particle concentration.

# Chapter 6

## CONCLUSIONS AND RECOMMENDATIONS

### 6.1. CONCLUSIONS

In the first part of our study, we investigated the effect of the aspect ratio of MWNTs on the viscoelastic and flammability properties of PS/MWNT. We employed two different types of MWNTs which had average aspect ratios of 49 and 150. These were determined by analyzing SEM and TEM images of the tubes extracted from the compounded nanocomposites. No significant effects of aspect ratio on thermal stability of PS/MWNT nanocomposites were observed. However, the viscoelastic properties were improved to a greater extent when the larger aspect ratio MWNTs were employed. Correspondingly, mass loss and heat release rates were decreased more in composites containing large aspect ratio MWNTs.

In the second part of our study, we have shown that the conductivity of PS/MWNT and PS/CNF nanocomposites is decreased as a result of processing (by twin-screw extrusion and compression molding), but can be recovered by annealing at high temperatures. Similarly, the dynamic rheological properties, specifically the elastic modulus  $G'$  at low frequencies, can also be increased by annealing. The microstructural basis for the above results is that, during processing, the particles become aligned in the flow direction, leading to a decrease in the connectivity of the particle network. The same connections, however, are re-established during annealing, which explains the recovery of the properties. Direct evidence for the above mechanism has been obtained by

confocal microscopy. We believe that our results may have practical relevance for the large-scale manufacture of conductive polymer nanocomposites.

In this study, we have presented a simple method to substantially improve the efficiency of clay particles as a nanoscale filler for polymers. We have shown that, by excluding the large particles and aggregates from a commercial clay, we can obtain a fractionated montmorillonite (FMT) that, when organically modified, disperses better into polystyrene. The resulting PS/o-FMT nanocomposites are more transparent and display significantly higher elastic moduli compared to PS nanocomposites prepared with an equivalent commercial organoclay. The flammability properties of the PS/o-FMT also appear to be slightly improved – in particular, greater amounts of residue are left behind when the materials are burned. The improvement in properties with the o-FMT is presumably because the particles are more effective at building a particle network, i.e., in terms of increasing the connectivity of the network. We suggest that the effectiveness of o-FMT particles should also extend to their dispersions in non-polar solvents, such as for the creation of greases and paints at a low particle concentration. The attractiveness of using o-FMT stems from the wide availability of MMT and the ease with which o-FMT is prepared from MMT.

## **6.2. RECOMMENDATIONS FOR FUTURE WORK**

Based on the studies we have reported, we suggest three feasible projects for future work, and these are briefly described below.

### **6.2.1. Flammability of Char Forming Polymers Containing MWNTs**

Polymers such as polyacrylonitrile (PAN) and polycarbonate (PC) do not burn to completion like the thermoplastic PS employed in this study. Instead, PAN and PC form large amounts of char during burning. Char forming polymers are widely used in applications where flammability reduction is required due to their char forming ability. We recommend that rheological and flammability studies of these materials be performed with and without the addition of nanoscale fillers such as MWNTs and clays. It will be interesting to see if char formation by PC and PAN polymers, and hence the flammability, is enhanced as a result of the addition of anisotropic nanoparticles. We expect synergy between the char forming polymer and nanoscale additive to result in highly useful flame retardant materials.

### **6.2.2. Properties of o-FMT Nanocomposites**

In many applications, high purity clays such as synthetic micas are employed due to the limitations of MMT dispersions. The attractiveness of o-FMT as an inexpensive alternative to synthetic clays stems from its ease of preparation, which does not involve any chemical synthesis except for a conventional surfactant treatment, and the wide availability of its MMT precursor. Whereas we have studied the flammability, rheological and transparency properties of composites containing o-FMT, other

properties remain to be studied. Specifically, it is quite possible that the exclusion of large aggregates from o-FMT that results in improvements in rheology and transparency may also lead to stiffer and less permeable composites. Whereas reduction in flammability metrics was not substantial, the effect of replacing 15A by o-FMT may be greater in the above mentioned composite properties.

### **6.2.3. Dispersions of o-FMT in Non-Polar Solvents**

Naturally occurring clay dispersions have eluded theoretical scrutiny due to the complexity of the naturally occurring clay samples which involve complex shapes and large size polydispersity. Theoretical predictions of the formation of liquid crystalline phases in dispersions of anisotropic particles have not been fulfilled in naturally occurring clays. In the preparation of o-FMT we eliminate one such complexity, namely, we remove large aggregates that exfoliate poorly. A key observation we made is that FMT gels in water display birefringence, which is usually indicative of alignment anisotropy. While this is a well studied effect in water, much less is known about the formation of liquid crystalline phases by organoclays in non-polar solvents. Thus, we recommend a systematic investigation of the addition of o-FMT to a variety of non-polar solvents and low molecular weight polymer melts to study both the enhancement of rheological properties as well as the possible occurrence of liquid crystalline phases.

## REFERENCES

- [1] Giannelis, E. P. "Polymer layered silicate nanocomposites." *Adv. Mater.* **1996**, *8*, 29-&.
- [2] Koerner, H.; Jacobs, D.; Tomlin, D. W.; Busbee, J. D.; Vaia, R. D. "Tuning polymer nanocomposite morphology: AC electric field manipulation of epoxy-montmorillonite (clay) suspensions." *Adv. Mater.* **2004**, *16*, 297-+.
- [3] Kashiwagi, T.; Du, F. M.; Douglas, J. F.; Winey, K. I.; Harris, R. H.; Shields, J. R. "Nanoparticle networks reduce the flammability of polymer nanocomposites." *Nat. Mater.* **2005**, *4*, 928-933.
- [4] Beyer, G. "Flame retardant properties of EVA-nanocomposites and improvements by combination of nanofillers with aluminium trihydrate." *Fire Mater.* **2001**, *25*, 193-197.
- [5] Hilding, J.; Grulke, E. A.; Zhang, Z. G.; Lockwood, F. "Dispersion of carbon nanotubes in liquids." *J. Dispersion Sci. Technol.* **2003**, *24*, 1-41.
- [6] Saito, R., Dresselhaus, G., Dresselhaus, M.S. *Physical Properties of Carbon Nanotubes*; Imperial College Press, 1998.
- [7] van Olphen, H. *An Introduction to Clay Colloid Chemistry*; John Wiley & Sons, Inc., 1963.
- [8] Davis, R. D.; Galman, J. W.; Sutto, T. W.; Callahan, J. H.; Trulove, P. C.; De Long, H. "Improved thermal stability of organically modified layered silicates." *Clay Clay Min.* **2004**, *52*, 171-179.
- [9] Giannelis, E. P.; Krishnamoorti, R.; Manias, E. Polymer-silicate nanocomposites: Model systems for confined polymers and polymer brushes. In *Polymers in Confined Environments*; Springer-Verlag Berlin: Berlin, 1999; Vol. 138; pp 107-147.
- [10] Macosko, C. W. *Rheology: Principles, Measurements and Applications*; VCH Publishers Inc., 1994.
- [11] Gilman, J. W.; Jackson, C. L.; Morgan, A. B.; Harris, R.; Manias, E.; Giannelis, E. P.; Wuthenow, M.; Hilton, D.; Phillips, S. H. "Flammability properties of polymer - Layered-silicate nanocomposites. Polypropylene and polystyrene nanocomposites." *Chem. Mat.* **2000**, *12*, 1866-1873.
- [12] Austin, P. J.; Buch, R. R.; Kashiwagi, T. "Gasification of silicone fluids under external thermal radiation part I. Gasification rate and global heat of gasification." *Fire Mater.* **1998**, *22*, 221-237.

- [13] Baughman, R. H.; Zakhidov, A. A.; de Heer, W. A. "Carbon nanotubes - the route toward applications." *Science* **2002**, *297*, 787-792.
- [14] Schadler, L. S.; Giannaris, S. C.; Ajayan, P. M. "Load transfer in carbon nanotube epoxy composites." **1998**, *73*, 3842-3844.
- [15] Stephan, C.; Nguyen, T. P.; Lahr, B.; Blau, W.; Lefrant, S.; Chauvet, O. "Raman spectroscopy and conductivity measurements on polymer-multiwalled carbon nanotubes composites." *J. Mater. Res.* **2002**, *17*, 396-400.
- [16] Dalton, A. B.; Collins, S.; Munoz, E.; Razal, J. M.; Ebron, V. H.; Ferraris, J. P.; Coleman, J. N.; Kim, B. G.; Baughman, R. H. "Super-tough carbon-nanotube fibres - These extraordinary composite fibres can be woven into electronic textiles." *Nature* **2003**, *423*, 703-703.
- [17] Barrau, S.; Demont, P.; Peigney, A.; Laurent, C.; Lacabanne, C. "DC and AC conductivity of carbon nanotubes-polyepoxy composites." *Macromolecules* **2003**, *36*, 5187-5194.
- [18] Thostenson, E. T.; Chou, T. W. "On the elastic properties of carbon nanotube-based composites: modelling and characterization." *J. Phys. D-Appl. Phys.* **2003**, *36*, 573-582.
- [19] Coleman, J. N.; Khan, U.; Blau, W. J.; Gun'ko, Y. K. "Small but strong: A review of the mechanical properties of carbon nanotube-polymer composites." *Carbon* **2006**, *44*, 1624-1652.
- [20] Moniruzzaman, M.; Winey, K. I. "Polymer nanocomposites containing carbon nanotubes." *Macromolecules* **2006**, *39*, 5194-5205.
- [21] Kashiwagi, T.; Grulke, E.; Hilding, J.; Harris, R.; Awad, W.; Douglas, J. "Thermal degradation and flammability properties of poly(propylene)/carbon nanotube composites." *Macromol. Rapid Commun.* **2002**, *23*, 761-765.
- [22] Beyer, G. "Short communication: Carbon nanotubes as flame retardants for polymers." *Fire Mater.* **2002**, *26*, 291-293.
- [23] Kashiwagi, T.; Grulke, E.; Hilding, J.; Groth, K.; Harris, R.; Butler, K.; Shields, J.; Kharchenko, S.; Douglas, J. "Thermal and flammability properties of polypropylene/carbon nanotube nanocomposites." *Polymer* **2004**, *45*, 4227-4239.
- [24] Peeterbroeck, S.; Alexandre, M.; Nagy, J. B.; Pirlot, C.; Fonseca, A.; Moreau, N.; Philippin, G.; Delhalle, J.; Mekhalif, Z.; Sporcken, R.; Beyer, G.; Dubois, P. "Polymer-layered silicate-carbon nanotube nanocomposites: unique nanofiller synergistic effect." *Compos. Sci. Technol.* **2004**, *64*, 2317-2323.

- [25] Schartel, B.; Potschke, P.; Knoll, U.; Abdel-Goad, M. "Fire behaviour of polyamide 6/multiwall carbon nanotube nanocomposites." *Eur. Polym. J.* **2005**, *41*, 1061-1070.
- [26] Gao, F. G.; Beyer, G.; Yuan, Q. C. "A mechanistic study of fire retardancy of carbon nanotube/ethylene vinyl acetate copolymers and their clay composites." *Polym. Degrad. Stabil.* **2005**, *89*, 559-564.
- [27] Kashiwagi, T.; Du, F. M.; Winey, K. I.; Groth, K. A.; Shields, J. R.; Bellayer, S. P.; Kim, H.; Douglas, J. F. "Flammability properties of polymer nanocomposites with single-walled carbon nanotubes: effects of nanotube dispersion and concentration." *Polymer* **2005**, *46*, 471-481.
- [28] Ashrafi, B.; Hubert, P.; Vengallatore, S. "Carbon nanotube-reinforced composites as structural materials for microactuators in microelectromechanical systems." *Nanotechnology* **2006**, *17*, 4895-4903.
- [29] Munsonmcgee, S. H. "Estimation of the Critical Concentration in an Anisotropic Percolation Network." **1991**, *43*, 3331-3336.
- [30] Gojny, F. H.; Wichmann, M. H. G.; Fiedler, B.; Kinloch, I. A.; Bauhofer, W.; Windle, A. H.; Schulte, K. "Evaluation and identification of electrical and thermal conduction mechanisms in carbon nanotube/epoxy composites." *Polymer* **2006**, *47*, 2036-2045.
- [31] Yang, Y.; Grulke, E. A.; Zhang, Z. G.; Wu, G. F. "Thermal and rheological properties of carbon nanotube-in-oil dispersions." *J. Appl. Phys.* **2006**, *99*.
- [32] Lu, C. S.; Mai, Y. W. "Influence of aspect ratio on barrier properties of polymer-clay nanocomposites." *Phys. Rev. Lett.* **2005**, *95*.
- [33] Osman, M. A.; Mittal, V.; Lusti, H. R. "The aspect ratio and gas permeation in polymer-layered silicate nanocomposites." *Macromol. Rapid Commun.* **2004**, *25*, 1145-1149.
- [34] Miyagawa, H.; Rich, M. J.; Drzal, L. T. "Amine-cured epoxy/clay nanocomposites. I. Processing and chemical characterization." *J. Polym. Sci. Pt. B-Polym. Phys.* **2004**, *42*, 4384-4390.
- [35] Stretz, H. A.; Paul, D. R.; Li, R.; Keskkula, H.; Cassidy, P. E. "Intercalation and exfoliation relationships in melt-processed poly(styrene-co-acrylonitrile)/montmorillonite nanocomposites." *Polymer* **2005**, *46*, 2621-2637.
- [36] Weon, J. I.; Sue, H. J. "Effects of clay orientation and aspect ratio on mechanical behavior of nylon-6 nanocomposite." *Polymer* **2005**, *46*, 6325-6334.

- [37] Kashiwagi, T. Flammability of nanocomposites: Effects of the shape of nanoparticles. In *Fire Retardancy of Polymers*; Le Bras, M., Wilkie, C. A., Bourbigot, S., Duquesne, S., Jama, C., Eds.; Royal Society of Chemistry: Cambridge, UK, 2005; pp 81-99.
- [38] Andrews, R.; Jacques, D.; Rao, A. M.; Derbyshire, F.; Qian, D.; Fan, X.; Dickey, E. C.; Chen, J. "Continuous production of aligned carbon nanotubes: a step closer to commercial realization." *Chem. Phys. Lett.* **1999**, *303*, 467-474.
- [39] Kashiwagi, T.; Fagan, J.; Douglas, J. F.; Yamamoto, K.; Heckert, A. N.; Leigh, S. D.; Obrzut, J.; Du, F. M.; Lin-Gibson, S.; Mu, M.; Winey, K. I.; Haggemueller, R. "Relationship between dispersion metric and properties of PMMA/SWNT nanocomposites" *Polymer* **2007**, *48*, 4855-4866.
- [40] Brauman, S. K. "Polymer Degradation During Combustion." *J. Polym. Sci. Pt. B-Polym. Phys.* **1988**, *26*, 1159-1171.
- [41] Kashiwagi, T.; Ohlemiller, T. J. "A Study of Oxygen Effects on Nonflaming Transient Gasification of PMMA and PE During Thermal Irradiation." *Proc. Combust. Inst.* **1982**, *19*, 815-823.
- [42] Treece, M. A.; Oberhauser, J. P. "Ubiquity of soft glassy dynamics in polypropylene-clay nanocomposites." *Polymer* **2007**, *48*, 1083-1095.
- [43] Wang, K.; Liang, S.; Deng, J. N.; Yang, H.; Zhang, Q.; Fu, Q.; Dong, X.; Wang, D. J.; Han, C. C. "The role of clay network on macromolecular chain mobility and relaxation in isotactic polypropylene/organoclay nanocomposites." *Polymer* **2006**, *47*, 7131-7144.
- [44] Gingold, D. B.; Lobb, C. J. "Percolative Conduction in 3 Dimensions." *Phys. Rev. B* **1990**, *42*, 8220-8224.
- [45] Kharchenko, S. B.; Douglas, J. F.; Obrzut, J.; Grulke, E. A.; Migler, K. B. "Flow-induced properties of nanotube-filled polymer materials." *Nat. Mater.* **2004**, *3*, 564-568.
- [46] Kashiwagi, T. "Polymer Combustion and Flammability - Role of the Condensed Phase." *Proc. Combust. Inst.* **1994**, *25*, 1423-1437.
- [47] Hu, G. J.; Zhao, C. G.; Zhang, S. M.; Yang, M. S.; Wang, Z. G. "Low percolation thresholds of electrical conductivity and rheology in poly(ethylene terephthalate) through the networks of multi-walled carbon nanotubes." *Polymer* **2006**, *47*, 480-488.

- [48] Yano, K.; Usuki, A.; Okada, A. "Synthesis and properties of polyimide-clay hybrid films." *J. Polym. Sci. Pol. Chem.* **1997**, *35*, 2289-2294.
- [49] Ramasubramaniam, R.; Chen, J.; Liu, H. Y. "Homogeneous carbon nanotube/polymer composites for electrical applications." *Appl. Phys. Lett.* **2003**, *83*, 2928-2930.
- [50] Smith, J. G.; Connell, J. W.; Delozier, D. M.; Lillehei, P. T.; Watson, K. A.; Lin, Y.; Zhou, B.; Sun, Y. P. "Space durable polymer/carbon nanotube films for electrostatic charge mitigation." *Polymer* **2004**, *45*, 825-836.
- [51] Potschke, P.; Abdel-Goad, M.; Alig, I.; Dudkin, S.; Lellinger, D. "Rheological and dielectrical characterization of melt mixed polycarbonate-multiwalled carbon nanotube composites." *Polymer* **2004**, *45*, 8863-8870.
- [52] Potschke, P.; Dudkin, S. M.; Alig, I. "Dielectric spectroscopy on melt processed polycarbonate - multiwalled carbon nanotube composites." *Polymer* **2003**, *44*, 5023-5030.
- [53] Lozano, K.; Bonilla-Rios, J.; Barrera, E. V. "A study on nanofiber-reinforced thermoplastic composites (II): Investigation of the mixing rheology and conduction properties." *J. Appl. Polym. Sci.* **2001**, *80*, 1162-1172.
- [54] Kota, A. K.; Cipriano, B. H.; Duesterberg, M. K.; Gershon, A. L.; Powell, D.; Raghavan, S. R.; Bruck, H. A. "Electrical and Rheological Percolation in Polystyrene/MWCNT Nanocomposites." *Macromolecules* **2007**, In Press.
- [55] Dalmas, F.; Chazeau, L.; Gauthier, C.; Masenelli-Varlot, K.; Dendievel, R.; Cavaille, J. Y.; Forro, L. "Multiwalled carbon nanotube/polymer nanocomposites: Processing and properties." *J. Polym. Sci. Pt. B-Polym. Phys.* **2005**, *43*, 1186-1197.
- [56] Du, F. M.; Fischer, J. E.; Winey, K. I. "Effect of nanotube alignment on percolation conductivity in carbon nanotube/polymer composites." *Phys. Rev. B* **2005**, *72*.
- [57] Du, F. M.; Scogna, R. C.; Zhou, W.; Brand, S.; Fischer, J. E.; Winey, K. I. "Nanotube networks in polymer nanocomposites: Rheology and electrical conductivity." *Macromolecules* **2004**, *37*, 9048-9055.
- [58] Sandler, J. K. W.; Kirk, J. E.; Kinloch, I. A.; Shaffer, M. S. P.; Windle, A. H. "Ultra-low electrical percolation threshold in carbon-nanotube-epoxy composites." *Polymer* **2003**, *44*, 5893-5899.

- [59] McNally, T.; Potschke, P.; Halley, P.; Murphy, M.; Martin, D.; Bell, S. E. J.; Brennan, G. P.; Bein, D.; Lemoine, P.; Quinn, J. P. "Polyethylene multiwalled carbon nanotube composites." *Polymer* **2005**, *46*, 8222-8232.
- [60] Alig, I.; Lellinger, D.; Dudkin, S. M.; Potschke, P. "Conductivity spectroscopy on melt processed polypropylene-multiwalled carbon nanotube composites: Recovery after shear and crystallization." *Polymer* **2007**, *48*, 1020-1029.
- [61] Xu, Y. J.; Higgins, B.; Brittain, W. J. "Bottom-up synthesis of PS-CNF nanocomposites." *Polymer* **2005**, *46*, 799-810.
- [62] van Ekenstein, G.; Meyboom, R.; ten Brinke, G.; Ikkala, O. "Determination of the Flory-Huggins interaction parameter of styrene and 4-vinylpyridine using copolymer blends of poly(styrene-co-4-vinylpyridine) and polystyrene." *Macromolecules* **2000**, *33*, 3752-3756.
- [63] Kita, R.; Kubota, K.; Dobashi, T. "Static and dynamic light scattering of a critical polydisperse polymer solution." *Phys. Rev. E* **1998**, *58*, 793-800.
- [64] Cipriano, B. H.; Kashiwagi, T.; Raghavan, S. R.; Yang, Y.; Grulke, E. A.; Yamamoto, K.; Shields, J. R.; Douglas, J. F. "Effects of aspect ratio of MWNT on the flammability properties of polymer nanocomposites." *Polymer* **2007**, In Press.
- [65] Bicerano, J.; Douglas, J. F.; Brune, D. A. "Model for the viscosity of particle dispersions." *J. Macromol. Sci.-Rev. Macromol. Chem. Phys.* **1999**, *C39*, 561-642.
- [66] Potschke, P.; Brunig, H.; Janke, A.; Fischer, D.; Jehnichen, D. "Orientation of multiwalled carbon nanotubes in composites with polycarbonate by melt spinning." *Polymer* **2005**, *46*, 10355-10363.
- [67] Ren, J. X.; Casanueva, B. F.; Mitchell, C. A.; Krishnamoorti, R. "Disorientation kinetics of aligned polymer layered silicate nanocomposites." *Macromolecules* **2003**, *36*, 4188-4194.
- [68] Solomon, M. J.; Almusallam, A. S.; Seefeldt, K. F.; Somwangthanaroj, A.; Varadan, P. "Rheology of polypropylene/clay hybrid materials." *Macromolecules* **2001**, *34*, 1864-1872.
- [69] Krishnamoorti, R.; Ren, J. X.; Silva, A. S. "Shear response of layered silicate nanocomposites." *J. Chem. Phys.* **2001**, *114*, 4968-4973.
- [70] Finnigan, B.; Jack, K.; Campbell, K.; Halley, P.; Truss, R.; Casey, P.; Cookson, D.; King, S.; Martin, D. "Segmented polyurethane nanocomposites: Impact of controlled particle size nanofillers on the morphological response to uniaxial deformation." *Macromolecules* **2005**, *38*, 7386-7396.

- [71] Maiti, P.; Yamada, K.; Okamoto, M.; Ueda, K.; Okamoto, K. "New polylactide/layered silicate nanocomposites: Role of organoclays." *Chem. Mat.* **2002**, *14*, 4654-4661.
- [72] Krishnamoorti, R.; Giannelis, E. P. "Rheology of end-tethered polymer layered silicate nanocomposites." *Macromolecules* **1997**, *30*, 4097-4102.
- [73] Abend, S.; Lagaly, G. "Sol-gel transitions of sodium montmorillonite dispersions." *Appl. Clay Sci.* **2000**, *16*, 201-227.
- [74] Pignon, F.; Magnin, A.; Piau, J. M. "Thixotropic behavior of clay dispersions: Combinations of scattering and rheometric techniques." *J. Rheol.* **1998**, *42*, 1349-1373.
- [75] Pignon, F.; Magnin, A.; Piau, J. M.; Cabane, B.; Lindner, P.; Diat, O. "Yield stress thixotropic clay suspension: Investigation of structure by light, neutron, and x-ray scattering." *Phys. Rev. E* **1997**, *56*, 3281-3289.
- [76] Raghavan, S. R.; Cipriano, B. H. Gel formation: Phase diagrams using tabletop rheology and calorimetry. In *Molecular Gelators and Their Gels*; Weiss, R. G., Terech, P., Eds.; Kluwer Publishers: Amsterdam, 2004.
- [77] Gabriel, J. C. P.; Sanchez, C.; Davidson, P. "Observation of nematic liquid-crystal textures in aqueous gels of smectite clays." *J. Phys. Chem.* **1996**, *100*, 11139-11143.
- [78] Ren, J. X.; Silva, A. S.; Krishnamoorti, R. "Linear viscoelasticity of disordered polystyrene-polyisoprene block copolymer based layered-silicate nanocomposites." *Macromolecules* **2000**, *33*, 3739-3746.
- [79] Wang, K. H.; Choi, M. H.; Koo, C. M.; Xu, M. Z.; Chung, I. J.; Jang, M. C.; Choi, S. W.; Song, H. H. "Morphology and physical properties of polyethylene/silicate nanocomposite prepared by melt intercalation." *J. Polym. Sci. Pt. B-Polym. Phys.* **2002**, *40*, 1454-1463.